*Article*

# Off-Stoichiometric Reactions at the Cell–Substrate Biomolecular Interface of Biomaterials: *In Situ* and *Ex Situ* Monitoring of Cell Proliferation, Differentiation, and Bone Tissue Formation

**Giuseppe Pezzotti** [1,2,3,4,*], **Tetsuya Adachi** [5] , **Francesco Boschetto** [1,4], **Wenliang Zhu** [1],
**Matteo Zanocco** [1,4], **Elia Marin** [1,5] , **B. Sonny Bal** [6] and **Bryan J. McEntire** [6]

[1]  Ceramic Physics Laboratory, Kyoto Institute of Technology, Sakyo-ku, Matsugasaki, Kyoto 606-8585, Japan
[2]  Department of Orthopedic Surgery, Tokyo Medical University, 6-7-1 Nishi-Shinjuku, Shinjuku-ku,
    Tokyo 160-0023, Japan
[3]  The Center for Advanced Medical Engineering and Informatics, Osaka University, 2-2 Yamadaoka, Suita,
    Osaka 565-0854, Japan
[4]  Department of Immunology, Graduate School of Medical Science, Kyoto Prefectural University of Medicine,
    Kamigyo-ku, 465 Kajii-cho, Kyoto 602-8566, Japan
[5]  Department of Dental Medicine, Graduate School of Medical Science, Kyoto Prefectural University of
    Medicine, Kamigyo-ku, Kyoto 602-8566, Japan
[6]  SINTX Technologies Corporation, 1885 West 2100 South, Salt Lake City, UT 84119, USA
*   Correspondence: pezzotti@kit.ac.jp; Tel.: +81-75-724-7568

check for
updates

**Abstract:** The availability of osteoinductive biomaterials has encouraged new therapies in bone regeneration and has potentially triggered paradigmatic shifts in the development of new implants in orthopedics and dentistry. Among several available synthetic biomaterials, bioceramics have gained attention for their ability to induce mesenchymal cell differentiation and successive bone formation when implanted in the human body. However, there is currently a lack of understanding regarding the fundamental biochemical mechanisms by which these materials can induce bone formation. Phenomenological studies of retrievals have clarified the final effect of bone formation, but have left the chemical interactions at the cell–material interface uncharted. Accordingly, the knowledge of the intrinsic material properties relevant for osteoblastogenesis and osteoinduction remains incomplete. Here, we systematically monitored *in vitro* the chemistry of mesenchymal cell metabolism and the ionic exchanges during osteoblastogenesis on selected substrates through conventional biological assays as well as via *in situ* and *ex situ* spectroscopic techniques. Accordingly, the chemical behavior of different bioceramic substrates during their interactions with mesenchymal cells could be unfolded and compared with that of biomedical titanium alloy. Our goal was to clarify the cascade of chemical equations behind the biological processes that govern osteoblastogenic effects on different biomaterial substrates.

**Keywords:** silicon nitride bioceramic; alumina bioceramic; titanium alloy; X-ray photoelectron spectroscopy; *in situ* Raman spectroscopy

## 1. Introduction

It is well established that bioceramics could be bioactive in terms of both osteoblastogenesis and osteoinductivity [1]. However, to acquire conclusive evidences that osteoinductive bioceramics can provide a valid alternative to autologous bone and osteogenic growth factors, a complete understanding of the chemical mechanisms behind the interaction between cells and the bioceramic surface is needed.

In this context, we notice that, within the field of biomaterials, it is common to classify oxide (e.g., alumina) and non-oxide ceramics (e.g., silicon nitride) as fully bioinert materials while only synthetic apatites and calcium phosphates are considered to be bioactive [1–3]. We shall instead provide clear evidence that those oxide and non-oxide ceramics are not bioinert. Conversely, they may be either supportive (bioactive) or detrimental to differentiation and metabolism of mesenchymal progenitor cells. After an initial proposal of osteoinductivity for calcium phosphate containing biomaterials [4,5], only one study has proposed osteoinductivity for alumina ceramics [6]; however, several studies have favored titanium as an osteoinductive substrate [7,8]. Recent *in vivo* and *in vitro* studies [9,10] have indicated that silicon nitride, a non-oxide bioceramic previously considered to be fully bioinert [1], is instead a formidable stimulator of osteoblastogenesis and osteoinductivity. The mechanisms of osteoinduction by the above biomaterials have been phenomenologically covered by the above publications, but the fundamental chemistry driving osteoblastogenesis and the successive bone formation needs additional elucidation. For more than 50 years bone biologists have embarked on efforts to understand the dynamic processes of differentiation and energetics of bone cells. However, the initial investigations of substrate utilization by bone cells were mainly focused on finely tuning the culture conditions for supporting collagen and mineral production [11]. Later, the focus shifted to hormonal regulation [12]. Currently, the search targets the role of substrates in anabolic treatments for osteoporosis and the enhancement of the work of the osteoblast through ionic alteration of osteoblast metabolism [13,14]. In this study, we re-examine and compare the surface chemistries of alumina, silicon nitride, and Ti6Al4V titanium alloy in this latter optics. Oxide and non-oxide bioceramics were selected for this investigation because they are presently used in joint arthroplasty and spine arthrodesis, respectively. Both bioceramics are considered as innovative choices with respect to titanium alloy, which is widely used in both the above applications. For this latter reason, we selected the Ti6Al4V alloy as the most appropriate substrate for comparative purpose.

The focus of this paper is on the ionic exchange at the interface between mesenchymal cells and different substrates. The aim of this study is to clarify which off-stoichiometric reactions take place at the biomolecular interface of bioceramics and how they differ between alumina ($Al_2O_3$) and silicon nitride ($Si_3N_4$) bioceramic substrates, demonstrating how the former stresses the cells in a similar way as titanium alloy, while the latter supports cell metabolism and bone formation.

## 2. Results

### 2.1. Substrate Surface Modifications in Aqueous Environment

The experiments described in this section challenge the notion that alumina oxide and silicon nitride non-oxide bioceramics remain completely inert in an aqueous environment. The substrate samples used in this study had surfaces with comparable average values of roughness: $0.32 \pm 0.02$, $0.10 \pm 0.01$, and $0.29 \pm 0.04$, for $Si_3N_4$, $Al_2O_3$, and Ti6Al4V alloy substrates, respectively. Figure 1a–c show the variations of X-ray photoelectron spectroscopy (XPS) Si2p core spectrum of silicon nitride, O1s core spectrum of Ti6Al4V alloy, and Al2p core spectrum of alumina with time in water vapor environment, respectively. The core spectra in the respective sections, which compare the as-received and 24 h-exposed surfaces, were deconvoluted into peak components representing the respective bonds, as shown by the labels of the figure [15–20]. The plots on the left side of each section give the trends with time of the population of individual bond components in terms of elemental fractions.

XPS data showed that all the investigated substrates underwent significant variations in their surface chemistry upon exposure to aqueous solution. As seen in Figure 1a, the Si2p core spectrum of silicon nitride could be deconvoluted into three peaks, which arose from [15]: N-Si-N (silicon nitride), N-Si-O (silicon oxynitride), and O-Si-O (silica) bond populations. As oxidation only affects the very surface of the material, the XPS probe, which is shallow at the single nanometer scale, was the most suitable probe to identify changes in surface chemistry. The N-Si-N peak component was preponderant on the pristine surface, but the surface exposed to water vapor environment showed a gradually

increasing amount of O-Si-O bonds, as seen in the plot on the left side of Figure 1a. The increase in relative intensity of the O-Si-O peak occurred at the expenses of the N-Si-N one. This represents an unequivocal proof of oxidation with the formation of a silica layer. Note that the presence of silicon oxynitride bonds was not significantly altered up to 48 h. The zeta potential value at homeostatic pH of the $Si_3N_4$ surfaces was −50 mV and tended to slightly higher negative values with increasing autoclaving time concurrently with the increase in population of O-Si-O bonds.
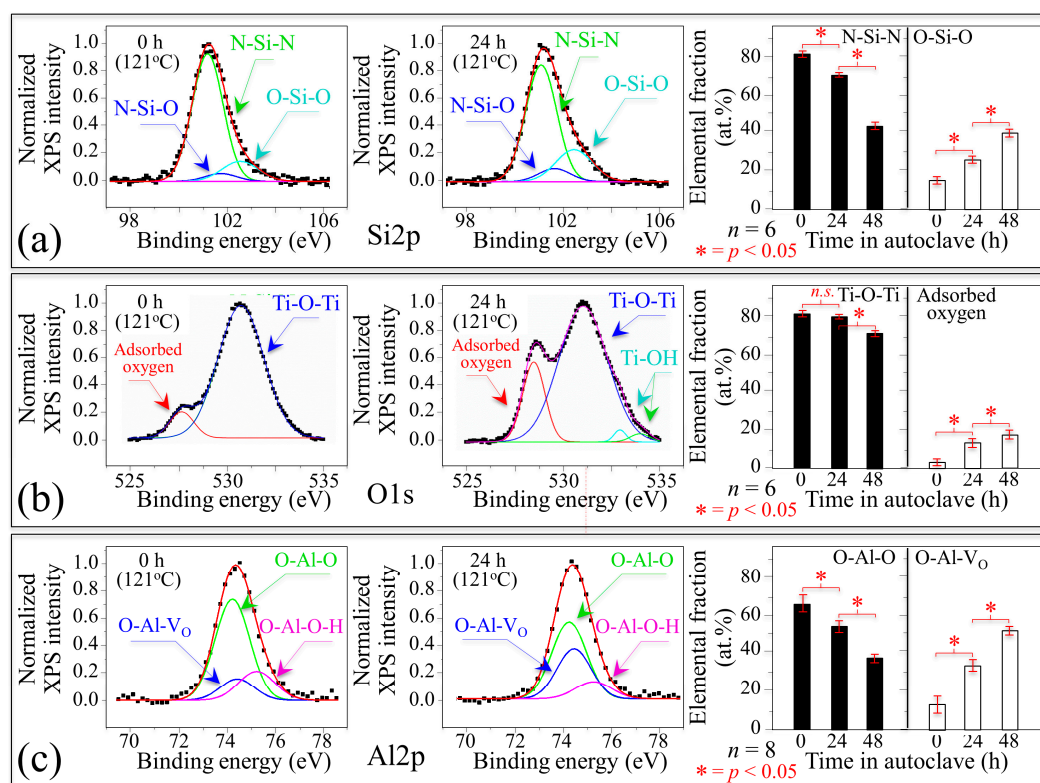


**Figure 1.** X-ray photoelectron spectroscopy (XPS) analyses of the investigated substrates before (left) and after (center) accelerated tests in water vapor environment, and plots summarizing elemental fraction results at different autoclaving times (right): (**a**) Si2p core spectrum of silicon nitride; (**b**) O1s core spectrum of Ti6Al4V alloy; and (**c**) Al2p core spectrum of alumina, with the related deconvolutions and quantitative time dependencies. Statistics were made according to the one-way Analysis of Variance (ANOVA) to assess the plots on the right side of each section.

The O1s core spectrum obtained by XPS measurement for the passive layer of the Ti6Al4V alloy substrate subjected to hydrothermal treatment, as seen in Figure 1b, was deconvoluted into four peaks according to Healy et al. [16,17] and Hierro–Oliva et al. [18]. The most pronounced peak, which can be seen at 531 eV, relates to oxygen atoms in the titanium oxide lattice; the peak at 532.9 eV belongs to the OH group. The Ti-O-Ti bridging oxygen bonds are proton-coordinated at the titanium oxide surface with oxygen from water molecules physically adsorbed on the titanium oxide surface. The peak displayed at 534.2 eV represents oxygen sites located at terminal Ti-OH bonds, for which the hydroxyl groups are chemically adsorbed on the titanium oxide surface. Finally, the peaks at 532.9 and 534.2 eV represent acidic and basic Ti-OH groups, respectively [19]. According to data in Figure 1b, a small population of both acidic and basic Ti-OH groups became present on the surface layer of the titanium alloy after hydrothermal treatment. The cumulative areal fraction of acidic and basic Ti-OH peaks remained small with increasing time of hydrothermal treatment. However, the presence of these peaks represented a strong indication that a small amount of anatase-type titanium oxide, which possesses both acidic and basic Ti-OH groups, formed on the surface of the titanium alloy substrate upon hydrothermal treatment. The most striking feature in the XPS spectrum of Ti6Al4V alloy subjected to

water vapor environment was the rising peak centered at 528.1 eV, which can be assigned to adsorbed atomic oxygen [20]. Such an adsorbed oxygen species is known to be electron rich oxygen, which has been proposed to activate C–H bond breaking [21,22]. The presence of such highly reactive species could participate in the partial oxidation of surrounding molecules. Specifically, it is possible that unwanted reactions take place at the cell–substrate interface, which is a typically reported issue for adsorbed atomic oxygen [23]. The zeta potential value at homeostatic pH of the Ti6Al4V alloy surfaces was −20 mV.

The behavior of alumina surface during the accelerated test in water vapor environment is shown in Figure 1c. The Al2p core spectrum of alumina was deconvoluted into three peak components: hydroxylated (O-Al-O-H) bonds, non-hydroxylated (O-Al-O) bonds, and O-Al-$V_O$ bonds representing the bond population at the material surface. A comparison between pristine and 24 h water-vapor-exposed samples revealed quick stoichiometric variations at the surface of the oxide substrate. A fraction of O-Al-$V_O$ bonds gradually replaced both O-Al-O and O-Al-O-H bonds. Water molecules experience different strengths when hydrogen bonds to oxide and non-oxide ceramic surfaces (i.e., aluminols in $Al_2O_3$-based and silanols in $Si_3N_4$ ceramics) [24]. In the silanols developed on the $Si_3N_4$ surfaces, H-bond acceptors were strong while H-bond donors were weak. Conversely, in the aluminols developed on the $Al_2O_3$ surfaces, H-bond donors were relatively strong and acceptors relatively weak. The nature of H-bonds is key in the dual role of a surface as solvent of oxidant. The fundamental difference between the acid character of surface silanols and the basic one of aluminols has important repercussions on the metabolism of mesenchymal cells exposed to different bioceramic substrates. The zeta potential value at homeostatic pH of the $Al_2O_3$ surfaces was +20 mV.

## 2.2. Mesenchymal Cell Proliferation and Differentiation

Figures 2 and 3 summarize data collected by fluorescence microscopy and other biological assays, and laser microscopy data collected on KUSA-A1 mesenchymal cells exposed to different substrates. These figures also provide statistically data validations. The fluorescence micrographs in Figure 2 (nuclei and F-actin in blue and green, respectively) confirmed that the population of KUSA-A1 cells was clearly more numerous on the $Si_3N_4$ substrates after exposure times as short as 24 h, as seen in Figure 1a, while the number of cells was far lower on Ti6Al4V alloy substrates, as seen in Figure 1b, and relatively low on $Al_2O_3$ substrates, as seen in Figure 1c. The plot in Figure 2d quantitatively compares cell-counting data for 24 h exposure to different substrates.

Assessments of differentiation and osteogenic metabolism in mesenchymal KUSA-A1 cells exposed for nine days to different substrates are given in Figure 3a–c. In Figure 3a,b, comparative plots of γ-carboxyglutamic (Gla)- and undercarboxylated (Glu)-osteocalcin, respectively, are given for cell-line exposure to different substrates. Statistically significant differences in concentration can be noticed in the Gla-osteocalcin plot, with the $Si_3N_4$ substrate reaching values more than one order of magnitude larger than and almost twice as those recorded for negative and positive control samples, i.e., cultured on silica glass without and with osteogenic medium, respectively, but otherwise under the same experimental conditions. The concentration of Gla-osteocalcin for mesenchymal cells exposed to the $Si_3N_4$ substrate was about 56% and 89% higher than those measured for exposures of cells to Ti6Al4V alloy and $Al_2O_3$ substrates, respectively. The Gla residue of osteocalcin is a specific and highly sensitive parameter for quantitative assessments of decarboxylated osteocalcin from the bony tissue produced by KUSA-A1 cells that differentiated into mature osteoblasts. Conversely, concentrations of the Glu residue, which is synthesized by osteoclasts, were the lowest in both $Si_3N_4$ and Ti6Al4V alloy substrates; no statistically significant difference between the two values was found but both were lower by ~40% and 30% than both positive and negative control, respectively. Note that the $Al_2O_3$ substrate experienced the lowest and the highest concentration of Gla- and Glu-osteocalcin supernatants, respectively, thus not only revealing the lowest propensity to osteoblastogenesis but also a conspicuous propensity for the mesenchymal cells to differentiate into mature osteoclasts.

Insulin-like growth factor 1 (IGF-1) signaling, as seen in Figure 3c, which can also be a probe for cell proliferation and differentiation efficiency, gave results comparable to those of the Gla-osteocalcin supernatant assay. The IGF-1 protein, which stimulates both differentiation and apatite growth, quantitatively probed a significantly higher metabolic propensity for the KUSA-A1 cells to differentiate into osteoblasts and subsequently generate more copious amounts of native apatite on $Si_3N_4$ when compared with Ti6Al4V alloy substrates. Conversely, the results of the IGF-1 assay in the plot of Figure 3c confirmed that mesenchymal cells cultivated on $Al_2O_3$ substrates possessed the lowest propensity to differentiate into mature osteoblasts. The IGF-1 supernatant concentration for cells exposed to the $Al_2O_3$ substrates was 93% and 32% lower than that detected for cell exposed to $Si_3N_4$ and Ti6Al4V substrates, respectively. The KUSA-A1 cells exposed to the $Si_3N_4$ substrate produced a IGF-1 concentration more than 300% higher than that of the positive control cell sample cultured on silica glass under the same conditions, not shown in the plot of Figure 3c. Figure 3d gives a quantitative estimate of the amount of bony apatite as obtained from laser microscopy assessments at the end of cell-culture experiments (14 days) on different substrates. As a conceivable consequence of the results collected by signaling assays at earlier stages of cell culture, the volumetric amount of bony apatite per unit area measured on $Si_3N_4$ substrates greatly exceeded those recorded for cultures on $Al_2O_3$ and Ti6Al4V substrates (170% and 87% higher, respectively).

Figure 4a shows the results of alkaline phosphatase (ALP) staining while micrographs showing the black ALP stain on the $Si_3N_4$, Ti6Al4V, and $Al_2O_3$ substrates at nine-day exposure time are shown in Figure 4b–d, respectively. The ALP content of cells cultured on the $Si_3N_4$ substrate was about twice that of cells cultured on the $Al_2O_3$ substrate under the same conditions; cells on the Ti6Al4V substrate showed the lowest ALP concentration among the investigated samples (~20% lower than cell on $Al_2O_3$). However, there was no statistical difference between the ALP contents measured in cells cultured on these two latter substrates. ALP is an enzyme that represents cell differentiation and the present results prove that the KUSA-A1 cells differentiated faster on the $Si_3N_4$ substrate, a result in agreement with the IGF-1 results in Figure 3c.
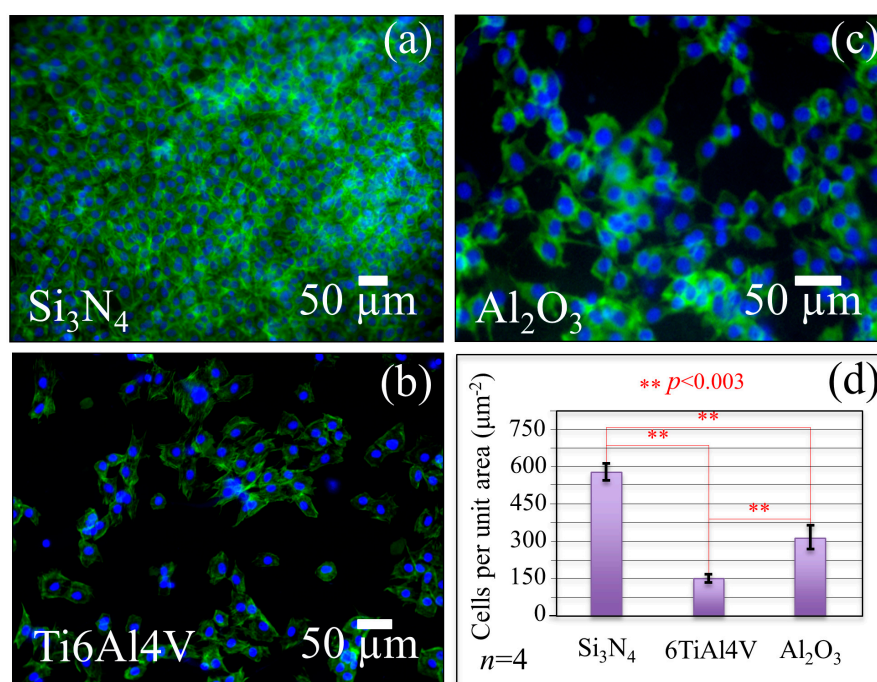


**Figure 2.** Fluorescence microscopy images of stained KUSA-A1 cells (nuclei and F-actin in blue and green, respectively) that proliferated for 24 h on (**a**) $Si_3N_4$, (**b**) Ti6Al4V alloy, and (**c**) $Al_2O_3$ substrates; in (**d**), quantitative plot and statistical validation of cell counting on different substrates. Statistics were made according to the one-way Analysis of Variance (ANOVA) to assess the plot in (**d**).
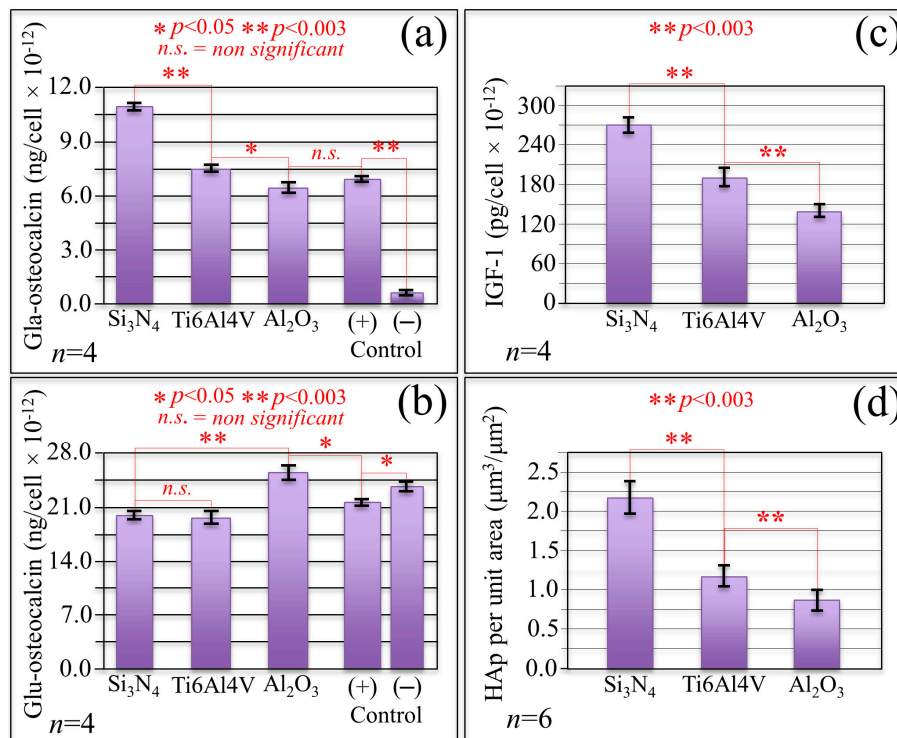
**Figure 3.** In (**a**) and (**b**), comparative plots of Gla- and Glu-osteocalcin, respectively, for cells exposed for nine days to different substrates; in (**c**), a similar evaluation is shown for IGF-1; (**d**) gives a plot of the volume per unit area of bony apatite grown by cells after exposure for 14 days to different substrates. Statistics were made according to one-way Analysis of Variance (ANOVA).
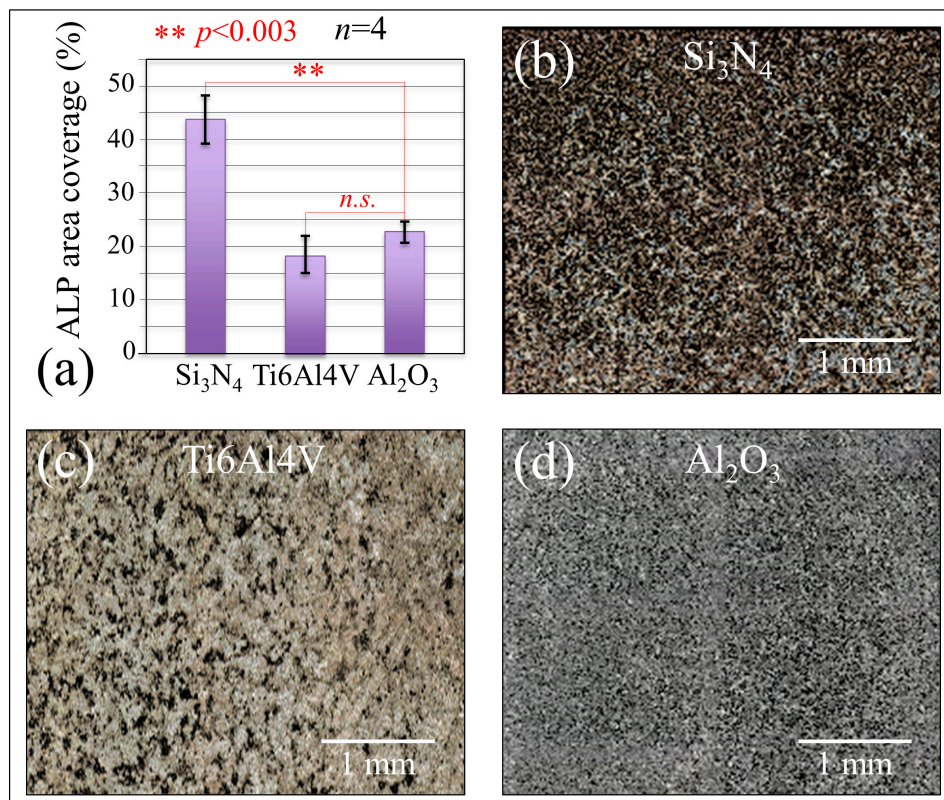


**Figure 4.** In (**a**), quantitative assessment of ALP concentration as obtained from stained micrographs on $Si_3N_4$ (**b**), Ti6Al4V (**c**), and $Al_2O_3$ (**d**).

## 2.3. In Situ Raman Analyses

Figure 5 shows the low-frequency Raman spectra collected in situ for: (a) the positive control cell sample (cultured on silica glass substrate for 48 h with addition of osteogenic medium), (b) after 48 h culture on $Si_3N_4$ substrate, (c) after 48 h culture on Ti6Al4V alloy substrate, and (d) after 48 h culture on $Al_2O_3$ substrate.
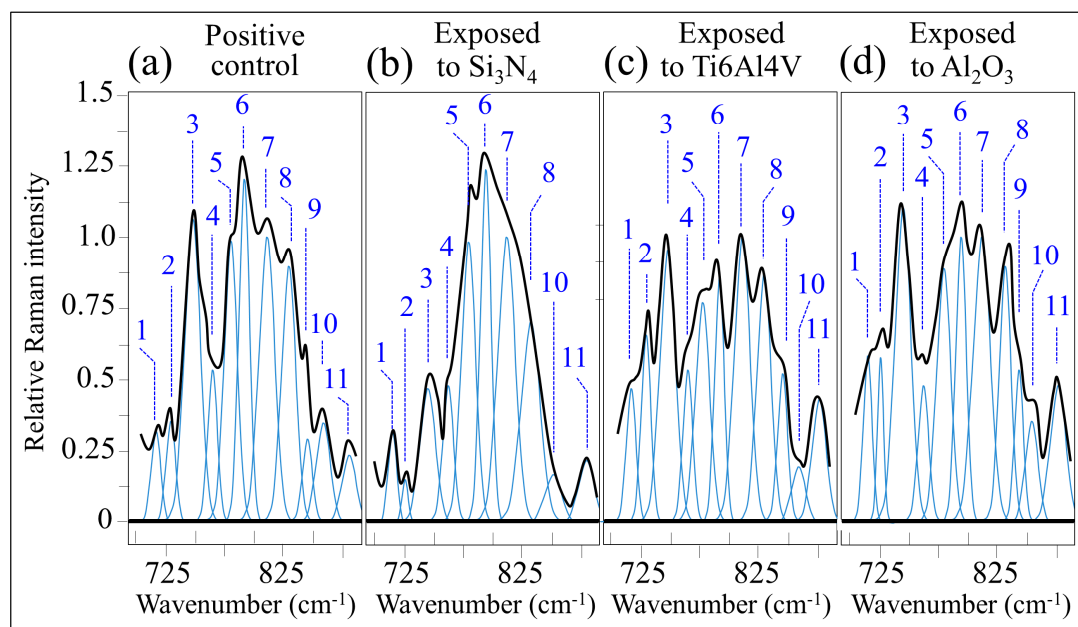


**Figure 5.** Low-frequency Raman spectra for (**a**) positive control cell sample, (**b**) cells exposed for 48 h to $Si_3N_4$ substrate, (**c**) cells exposed for 48 h to Ti6Al4V alloy substrate, and (**d**) cells exposed for 48 h to $Al_2O_3$ substrate. All the spectra were normalized to Band 7 (at 813 $cm^{-1}$, related to symmetric stretching of the phosphodiester bonds of RNA [25–27]).

Eleven Raman bands were located in the monitored spectral window, the precise frequencies of which as well as their physical origins have been reported in a previous paper [10]. In the case of cells cultured on $Si_3N_4$ substrates, no significant variations in relative intensity when compared with the positive control sample could be observed after 48 h for RNA/DNA-related Bands 5 (at 783 $cm^{-1}$), 6 (at 794 $cm^{-1}$), and 7 (at 813 $cm^{-1}$). These bands represented vibrations of phosphodiester symmetric stretching in DNA, ring breathing in cytosine, and phosphodiester symmetric stretching in RNA, respectively [25–27]. An exception among nucleic acid related bands was Band 8 (out-of-plane ring breathing in tyrosine [28]), which showed a clear decrease of approximately 20% in relative intensity in the spectrum collected on cells exposed to $Si_3N_4$ substrates in compared with control, as seen in Figure 5a,b. Conversely, the decrease in cytosine band was by far less pronounced in the case of cells cultured on both Ti6Al4V and $Al_2O_3$ substrates, as seen in Figure 5c,d, respectively. The decrease in relative intensity of Band 8, which reflects a reduction in tyrosine content, was consistent with the observation of a concurrent decrease in intensity of Band 10 (at 852 $cm^{-1}$) related to tyrosine (benzene ring breathing [29]) but also contributed by O-P-O stretching in adenosine triphosphate. A striking additional feature in the spectrum of $Si_3N_4$-exposed cells when compared with the control was a dramatic decrease of the tryptophan Band 3 (at 748 $cm^{-1}$) [26]. This feature could neither be detected in the Ti6Al4V nor in the $Al_2O_3$ substrates, as seen in Figure 5b,c, respectively. Other characteristics peculiar to the spectrum of mesenchymal cells exposed to $Si_3N_4$ substrates were: (i) the disappearance of a sharp shoulder Band 9 (at 843 $cm^{-1}$) mainly related to phosphatidylinositol [30]; (ii) a clear decrease in relative intensity (and shift from 733 to 726 $cm^{-1}$) of Band 2 (at 733 $cm^{-1}$), which is a composite signal of phosphatidylserine (C-N stretching in the serine residue [30]) and adenosine triphosphate (adenine ring breathing [31,32]). The above variations of Bands 8, 10, 3, 9, and 2 are clear fingerprints of an altered

cell metabolism that have only occurred upon short-term exposure to the $Si_3N_4$ substrate. The sacrificial reductions in the selected tryptophan purine, adenosine triphosphate, and protein tyrosine, as well as the clear alteration in phospholipids' composition, i.e., disappearance of the phosphatidylinositol band and reduction in phosphatidylserine, are clear signs of osteoblastogenesis. Evidences obtained through comparative data on control samples and samples exposed to different substrates are also consistent with the thesis of an enhanced propensity to differentiation into osteoblasts as a consequence of cell–substrate interactions at the molecular scale. In particular, the decrease in relative intensity of the tyrosine ring breathing Bands 8 and 10 is a consequence of nitration in tyrosine proteins by NO radicals [33]. During osteoblastogenesis, the so-called kynurenine pathway is activated [34]. In this pathway, cells utilize tryptophan to synthesize proteins after cleaving its indole ring [35]. Tryptophan is a precursor in the synthesis of melatonin, which increases differentiation of human mesenchymal stem cells into the osteoblastic cell lineage [36]. Moreover, the reduced intensity of Band 2, to approximately a third of that of the control cell sample, and its shift toward lower frequencies can be interpreted as the spectroscopic fingerprints of deprotonation from $-NH_3^+$ to $-NH_2$ in the serine group of the phosphatidylserine lipid structure of the cell membrane. Under the effect of alkaline phosphatase, calcium concentration increases in the cytoplasmic space, and $Ca^{2+}$ ions binds to the $COO^-$ terminus of the deprotonated serine residue forming Ca complexes [37]. Regarding the effect on other membrane lipids, the disappearance of the phosphatidylinositol Band 9 relates to the interaction between nitrogen radicals eluted from the $Si_3N_4$ substrate and the phosphate group of the inositol structure via transfer of $H^+$ protons. Conversely, the structure of phosphatidylcholine (represented by Bands 1 and 11 at 718 and 876 $cm^{-1}$, respectively [30]) remains unaffected because the choline ring in this phospholipid is neutral in nature. The chemical aspects of the interactions between mesenchymal cells and the $Si_3N_4$ substrate will be discussed in detail in the next section.

Despite some similarities with the spectrum of the control cell sample, distinct spectral features could be observed in the Raman spectra of mesenchymal cells exposed to Ti6Al4V and $Al_2O_3$ substrates, which could not be observed for cells cultured on $Si_3N_4$ substrates. In the spectrum of cells exposed to Ti6Al4V and $Al_2O_3$ substrates, the relative intensities of tryptophan-contributed Bands 3 and 4 remained comparable to that of the corresponding bands in the spectrum of the control sample. On the other hand, signals related to lipids (i.e., the Bands 1, 2, 9, and 11 contributed by C-N stretching in choline, C-N stretching in serine, cumulative signals from phosphatidylcholine and phosphatidylinositol, and C-N antisymmetric stretching in choline, respectively) experienced an increase in their relative intensities. Conversely, the two DNA-related Bands 5 and 6 (seen at 783 and 794 $cm^{-1}$, respectively) were of lower relative intensities when compared with the control cell sample and to the cell sample exposed to $Si_3N_4$ substrate, whose 5 and 6 signals were similar to those in the control; however, such intensity reductions were slightly more pronounced for the case of Ti6Al4V than for $Al_2O_3$ substrates. In a recent paper, Brauchle et al. [38] monitored the Raman spectra of apoptotic osteosarcoma and chondrosarcoma cell lines *in situ*. For both cell lines, the DNA signals at approximately 780~800 $cm^{-1}$ decreased during apoptosis. The authors suggested that such a decrease was related with to progress of internucleosomal DNA cleavage. Analogous to that study, one could also interpret the spectral changes observed in the Raman spectra of the present KUSA-A1 mesenchymal cells exposed to both Ti6Al4V alloy and $Al_2O_3$ substrates as fingerprints of intracellular biochemical changes correlated to toxic challenges [39]. The exogenous development of reactive oxygen species (ROS) at the biomolecular interface between cells and substrate could be one possible cause of irreversible damages to proteins and nucleic acids as well as the peroxidation of membrane lipids, which can lead to activation of cell death processes such as apoptosis [40]. The chemical origin of these processes detrimental to cell proliferation and osteoblastic activity will be discussed in detail in the next section.

## 3. Discussion

### 3.1. Off-Stoichiometric Reactions at the Cell–Substrate Interface

Figure 6 shows schematic drafts of the free surface of the investigated substrates and the set of off-stoichiometric reactions involved with their embedment in an aqueous solution.
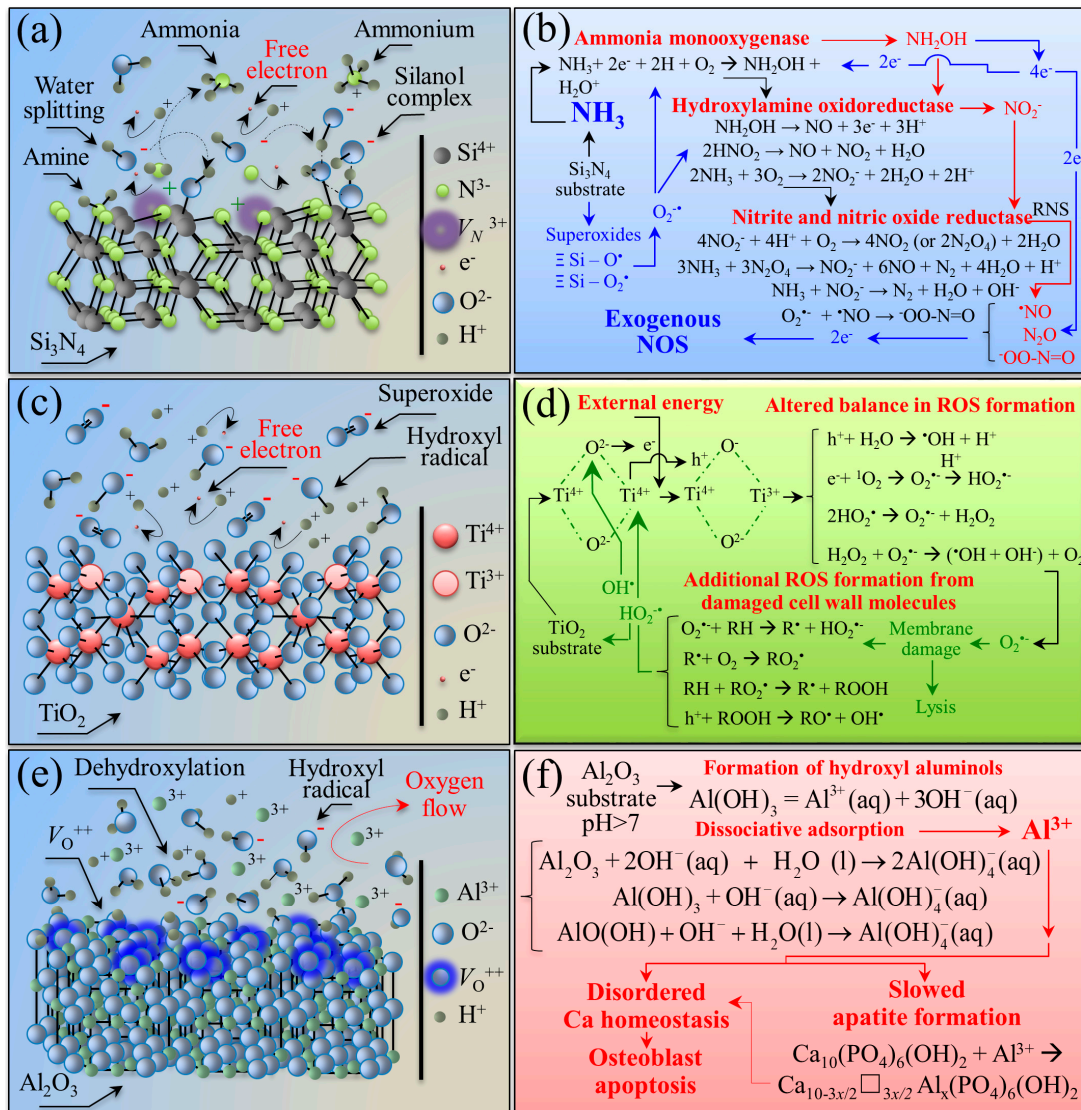


**Figure 6.** Schematic drafts of the free surface of different substrates in aqueous environment ($Si_3N_4$, Ti6Al4V alloy, and $Al_2O_3$ in (**a,c,e**), respectively) and the cascade of related off-stoichiometric reactions ($Si_3N_4$, Ti6Al4V alloy, and $Al_2O_3$ in (**b,d,f**), respectively).

The drafts and the reactions listed in the figure are based on the results of accelerated tests in water vapor provided in Section 3.1 and works published by these and other authors [41–47]. The behavior of $Si_3N_4$ bioceramic is described in Figure 5a,b. In aqueous solution, the surface lattice of this non-oxide ceramic is subjected to dissociation of its Si-N covalent bond. Such a homolytic bond cleavage liberates nitrogen ions to the environment, creates a nitrogen vacancy $V_N^{3+}$, and exposes silicon sites on the free surface. The former ions immediately join hydrogens in solution to form free ammonium ions $NH_4^+$ or ammonia $NH_3$; simultaneously, the latter ions find a new equilibrium state upon linking to OH ions to form silicon dioxide $SiO_2$ that further reacts with water and produces stable silanol structures $Si(OH)_4$ on the bioceramic surface, as seen in Figure 6a. A straightforward outcome for the

elution of nitrogen and the consequent formation of $NH_4^+/NH_3$ at the solid–liquid interface is a robust enhancement of local pH [48,49]. XPS data in accelerated water vapor environment confirmed this tendency, as seen in Figure 1a, showing increasing amounts of N-Si-O and O-Si-O bond populations at the expenses of the N-Si-N one. An important aspect of the hydrolysis process at the $Si_3N_4$ surface is that dissociation of both surface amine and silanol sites eventually generates free electrons and oxygen/nitrogen free radicals [41–43]. The off-stoichiometric chemical reactions of the newly formed species with the available free electrons ultimately lead to the formation of NO radicals, which have been experimentally observed and measured *in situ* in a previous work [44]. The cascade of off-stoichiometric reactions shown in Figure 6b can be explained with the dissociation of surface silanols as the initial step in the formation of superoxide radicals ($\equiv Si - O^\bullet$) and ($\equiv Si - O^\bullet_2$). Unpaired electrons can then react with adsorbed $O_2$ to form $O_2^{-\bullet}$ radical anions or other protonated radicals with highly oxidative characteristics. These species could, in turn, react with $NH_3$, leading to its oxidation into hydroxylamine ($NH_2OH$), according to a process referred to as ammonia monooxygenase. The availability of two free electrons from ammonia enables additional reductant contributions, according to which the second O atom forms $H_2O$ and leads to further oxidation of $NH_2OH$ into nitrite ($NO_2^-$). This process, which is referred to as hydroxylamine oxidoreductase, releases four electrons, two of which can promote further ammonia oxidation. Note that, in eukaryotic cells, the mitochondrion is also a major source of oxygen radicals with the transfer of four electrons to an $O_2$ molecule made possible through cytochrome c oxidase enzymatic catalysis. However, this process is accompanied by the eventual formation of byproducts of partially reduced species as a consequence of leakage from transport chains of the electrons associated with the transfer [45]. The availability of the leaked free electrons can also serve to neutralize small infiltrations of exogenous $NH_3$ through the cell plasma membrane by oxidizing it into hydroxylamine $NH_2OH$. Additional gaseous reactive nitrogen species (RNS) products of $NH_3$ oxidation are NO and $^-OONO$, which are also highly reactive and oxidative species [46]. The successive off-stoichiometric events of monooxygenase, oxidoreductase, and the formation of gaseous oxidizing byproducts originate from the concurrent presence of ammonia and silanols, and are thus peculiar to the $Si_3N_4$ surface in aqueous environment. Among the exogenously produced RNS at the biomolecular interface between cells and the $Si_3N_4$ substrate, NO covers a fundamental role in cell signaling. Specifically regarding the topic of the present work, as a reactive byproduct of ammonia and ammonium, exogenous nitric oxide NO can participate in enzymatic reactions and displace osteoblastogenesis and glutamine synthetase equilibriums [47]. Note that the elution of nitrogen and the successive formation of $NH_4^+/NH_3$ locally enhance pH at the cell–substrate interface, as experimentally demonstrated in previous papers [48,49]. Such a pH buffering process boosts alkaline phosphatase (ALP) with calcium concentration locally increasing and $Ca^{2+}$ binding to the $COO^-$ terminus of the deprotonated serine residue to form Ca complexes. This interpretation fits both the present ALP results (Figure 4) and the lipid structural alterations recorded in the Raman data of Figure 5a.

Figure 6c,d give a schematic draft of the free surface of the Ti6Al4V alloy substrate and the set of off-stoichiometric reactions involved with its embedment in aqueous solution, respectively. A previous study by Jennison et al. [50] has shown that a $TiO_2$ passivation layer naturally forms on Ti6Al4V alloy. One reason why the Ti6Al4V alloy is widely used in biomedical implants is that its $TiO_2$ surface layer possesses antibacterial efficacy, a property exploited in advanced biomedical technologies [51]. The chemical circumstance behind this property is the free-radical effect of the passivation $TiO_2$ layer [52–54]. However, despite the wide attention given to the antibacterial properties of titanium alloys, studies on the effect of their surface chemistry on cells have seldom been published.

The $TiO_2$ surface of Ti6Al4V alloy can change into TiOH metastable intermediates, as seen in Figure 6c, a process that is greatly enhanced by ultraviolet light irradiation but can partly take place also in dark environments [55]. The origin of the charge at the $TiO_2$ surface resides in the formation of oxygen vacancies consequential to a reductive change in valence from $Ti^{4+}$ to $Ti^{3+}$ [56]. Figure 6d summarizes the oxygen radical chemistry pathways at the surface of the $TiO_2$ passivation layer.

Electrons $e^-$ and holes $h^+$ are generated which lead to dissociative chemisorption of water from the environment. In this study, the occurrence of the chemisorption process has directly been observed through XPS analyses, as seen in Figure 1b. The consequence of water chemisorption is the release of reactive oxygen species (ROS), such as hydroxyl radicals ($^{\bullet}OH$), superoxide ($O_2^{-\bullet}$), singlet oxygen ($^1O_2$), and hydrogen peroxide ($H_2O_2$) from the $TiO_2$ substrate [57]. The generated holes and electrons, precursors to the formation of ROS, recombine with free electrons to form new $O_2^{-\bullet}$ and $H_2O_2$. At the interface with prokaryotic cells, such highly oxidative radicals interact with the membrane species to produce degraded species and additional ROS. Unlike the relatively less active $O_2^{-\bullet}$ and $H_2O_2$, which can be detoxified through both enzymatic and non-enzymatic endogenous antioxidants, no enzyme can detoxify $^{\bullet}OH$ and $O_2^{-\bullet}$, and they induce extremely acute effects on bacteria [45,58]. However, the same circumstances that render ROS acutely lethal to bacteria might also lead to self-propagating chain reactions that ultimately lead to cell lysis. In this study, *in situ* collected Raman data on mesenchymal cells exposed to Ti6Al4V alloy substrates suggest molecular interactions at the cell–substrate interface that are not of a friendly nature. Spectroscopic features point at DNA damage and metabolic reactions in membrane lipids as fingerprints of incipient apoptosis induced by ROS.

Figure 6e,f show a schematic draft of the free surface of the $Al_2O_3$ substrate in aqueous environment and a set of related off-stoichiometric reactions, respectively. The surface of $Al_2O_3$ contains both acid and basic sites depending on the termination of the bulk surface, namely the exposure of metal cations for Lewis acid sites or oxygen atoms for Lewis and Brønsted basic sites. Minimization of the surface free energy takes place upon producing terminations with hydroxyl groups. Pure alumina contains only one type of cation and the hydroxyl groups at its surface are expected to be weakly to moderately acidic (due to the high ionicity of the Al–O bond) and, thus, to form weak hydrogen bonds with sorbed molecules. Hydroxyl groups might eventually be removed from the alumina surface upon thermal-frictional activation, and coordinatively unsaturated (oxygen) anions and exposed $Al^{3+}$ cations (and anion vacancies, $V_O^{2+}$) are formed on the surface. The formation of oxygen vacancies at the expenses of O-AlO bonds has been observed in this study by XPS analyses applied to substrate subjected to accelerated thermal activation, as seen in Figure 1c. In this context, the removal of OH groups happens concurrently with the development of OH site basicity, because the net positive charge at the anion vacancy becomes lower as the net negative charge of the removed OH group rises. Proton acidity and OH group removal are key factors in governing dehydroxylation, and they play a fundamental role on the "degree of bioinertness" of the oxide bioceramic surface, as seen in Figure 6e. Note that the coordinatively unsaturated Al ions represent strong electron acceptors (Lewis acid) sites for dissociative adsorption of water [59]. This process involves charge transfer from the $Al_2O_3$ cluster to hydroxyl, oxygen, and proton radicals, and is more energetically favorable than molecular adsorption, in which $H_2O$ donates its charge to the $Al_2O_3$ cluster [60,61]. Figure 6f shows the cascade of events taking place at physiological pH on an $Al_2O_3$ substrate. The process starts with the formation of hydroxyl aluminols, eventually followed by dissociative adsorption of the aluminols to liberate $Al^{3+}$ and $OH^-$ ions in solution. The removal of hydroxyl groups involves the formation of oxygen vacancies, with the OH groups being easily removed as a consequence of OH site basicity (i.e., the net remaining positive charge at anion vacancy site is lower than the net negative charge on the removed OH group). There are two consequences of dissociative adsorption at the $Al_2O_3$ surface. On the one hand, $Al^{3+}$ inhibits mineralization by slowing the rate of hydroxyapatite crystal formation, as seen in the chemical equations for the Al-modified apatite structure in Figure 6f, and altering the influx and efflux of calcium from bone cells [62]. On the other hand, the presence of $Al^{3+}$ could lead to oxidative stress through the formation of ROS with a significant perturbation of the normal anti-oxidative system [63]. Chambers and LoGrasso [64] reported *in vivo* and *in vitro* data showing that Al-induced oxidative stress activates cell apoptosis signaling pathways. The induction of oxidative stress by ROS is one of the toxic effects involved with the exposure of cells to aluminum, and its consequences include irreversible modifications of cellular proteins, lipids, and DNA [65]. A recent *in vitro* experimental study by Li et al. [66], which specifically targeted the oxidative injuries induced by aluminum to

osteoblasts, showed that the osteoblast apoptosis occurred within 24 h exposure and its rate increased with increasing the aluminum dose (in the order of $10^{-2}$ mg/mL). Membrane lipid rigidification occurs through chemical interaction between $Al^{3+}$ ions and the phosphate groups of phospholipids, which greatly limits cell mobility. The results were thus straightforward in proving that Al exposure causes significantly oxidative stress to induce apoptosis and injuries in osteoblasts. The results of the present experiments are in line with the above-cited studies. Although the kinetics of dissociative adsorption at the $Al_2O_3$ surface should be much slower in terms of aluminum elution than the direct doping experiments proposed in Refs. [62–66], yet we observed significant inhibition in osteoblastogenesis and a very low propensity to deposit bony apatite on $Al_2O_3$ when compared with other substrates. Remarkably, also *in situ* Raman experiments conducted after short-term exposure of mesenchymal cells to $Al_2O_3$ substrates provided molecular scale fingerprints, which could be interpreted as an apoptotic tendency of the mesenchymal cells.

### 3.2. RNS Formation and the Cell-Friendly Kinetics of Silicon Nitride

In mesenchymal cells, the isoenzymes referred to as endothelial (eNOS) and inducible (iNOS) are responsible for the production of NO, a short-lived and extremely volatile molecule that regulates both cell survival and death. Capable of freely passing through the cell membrane, NO is an intercellular messenger whose message is internalized through guanylate cyclase, a lyase enzyme that regulates the intracellular calcium level [67]. At low concentrations, NO is used by cells for signaling enhanced proliferation; however, in high concentrations, it causes apoptosis. In the clinical practice, NO can be generated, irrespective of production in the cells, by exploiting synthetic compounds such as sodium nitroprusside. This exogenous donor produces NO upon reacting with sulphydryl groups of the erythrocyte membrane, albumin, and other proteins via non-enzymatic and enzymatic processes [68]. Extensively used as a venous vasodilator, sodium nitroprusside serves to immediately decrease the blood pressure in critical clinical situations [69]. The efficacy of exogenous NO on the *in vitro* osteogenic differentiation of mesenchymal stem cells has been the object of a recent study by Abnosi and Pari [70]. These researchers discovered that low concentrations of exogenous sodium nitroprusside (in the order of <0.1 mM generating ~1.2 nM of NO) promoted the ability to proliferate and the capacity to differentiate into osteoblasts of rat bone marrow mesenchymal stem cells. This effect was attributed to an up-regulation by NO of alkaline phosphatase, the critical enzyme that releases the phosphate and causes calcium ions to enter the cells and form apatite. Conversely, concentrations in the order of 1 mM significantly reduced cell viability, an effect also contributed to by the concurrent release of cyanide and iron as toxic byproducts of NO synthesis from exogenous sodium nitroprusside compound. Cyanide is a toxic compound that inhibits cytochrome c oxidase in the cell respiratory chain [71]; inorganic iron has also been reported to inhibit the process of mineralization [72]. Sodium nitroprusside also generates ROS, which induce lipid peroxidation and cytotoxicity [73].

One of the key findings of the present study was the promotion of both proliferation and osteoblastogenesis of mesenchymal KUSA-A1 cells, which appears to be greatly enhanced when the cells are exposed to $Si_3N_4$ substrates. Biological assays probing for cell proliferation, as seen in Figure 2, differentiation, as seen in Figure 3a–c, and bony apatite production, as seen in Figure 3d, unequivocally showed a consistent picture of up-regulated osteogenesis as a consequence of the peculiar surface chemistry of $Si_3N_4$ bioceramics. During differentiation, mesenchymal cells utilize both oxidative phosphorylation and glycolysis pathways [74]. From a biochemical point of view, the initially high adenosine triphosphate level tends to linearly decrease upon cell differentiation in favor of increased diphosphate and monophosphate levels because released phosphate groups are needed for reaction with $Ca^{2+}$ to synthesize hydroxyapatite crystals [75]. A decrease in bands contributed by adenosine triphosphate, which reflects a decreased intracellular concentration of this compound, was observed by *in situ* Raman spectroscopy, as seen in the decrease in Bands 2 and 10 in Figure 5b in comparison with the control sample in Figure 5a. The exogenous production of NO at the cell/$Si_3N_4$ interface has been explained in Figure 6a,b, according to a cascade of reactions originated from surface hydrolysis

and including ammonia monooxygenase, hydroxylamine oxidoreductase, and nitrite/nitric oxide reductase. According to the obtained results, the NO amount released from the $Si_3N_4$ substrate appears to be low and slow enough to fall into the concentration range within which it operates as a signal for enhancing proliferation. A further important characteristic of the exogenous NO production from a $Si_3N_4$ surface is the absence of any toxic byproduct, different from the case of cyanide and iron ions released by the sodium nitroprusside donor. The only ionic byproduct of $Si_3N_4$ surface hydrolysis (beside nitrogen) is silicon, which is also an element that gives a positive contribution to osteogenesis [76,77]. $(SiO_4)^{4-}$ tetrahedra and Si nanodots were found in the structure of bony tissue grown both *in vitro* and *in vivo* by human osteoblasts in proximity of $Si_3N_4$ surfaces [44,78]. With regard to the differentiation of mesenchymal cells, osteoblast and osteoclast functions are regulated by the so-called NF-κB, a set of multifunctional transcriptional factors controlling the expression of the genes involved with skeletal development (among numerous other cellular activities) [79]. Figure 7 gives a schematic draft of NF-κB activation in response to a state of bone resorption or as a consequence of a reduced mechanical stimulus.
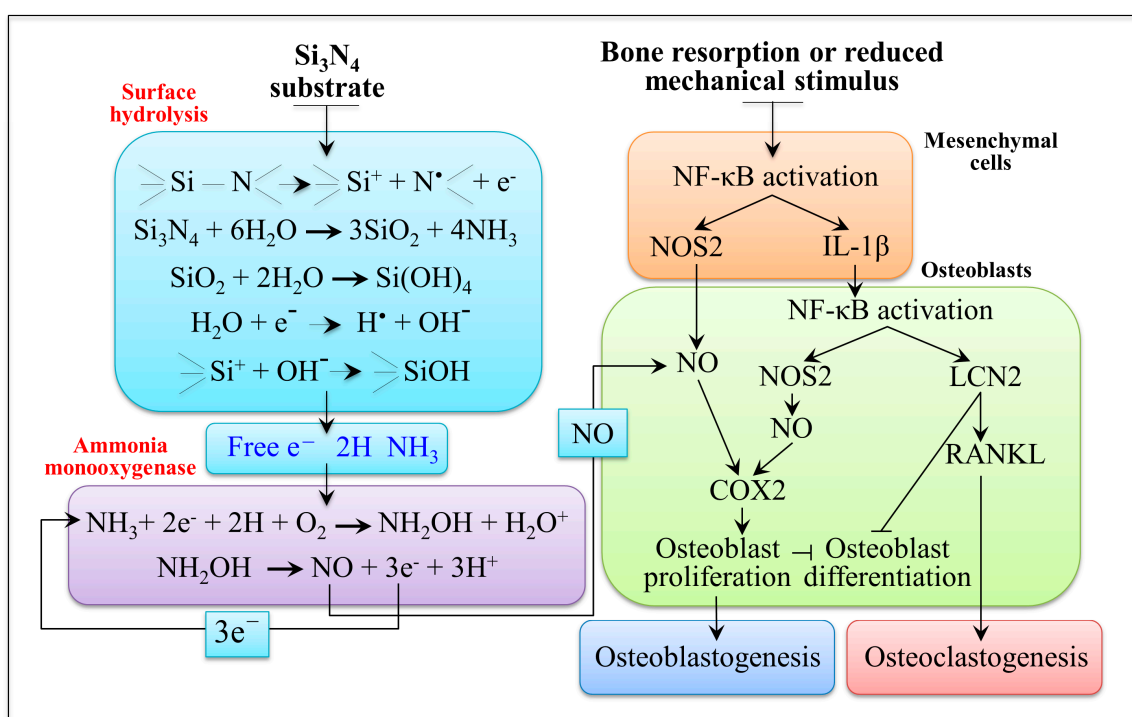


**Figure 7.** Schematic representation of the pathways involved with osteoblast-osteoclast crosstalk (IL-1β/LCN2/RANKL pathway leading to osteoclastogenesis and NOS2/NO/COX2 pathway leading to osteoblastogenesis); an exogenous NO uplift represents the final effect of RNS formed at the cell/$Si_3N_4$ interface as a consequence of hydrolysis and the subsequent cascade of chemical reactions taking place on the $Si_3N_4$ substrate in aqueous environment.

There are two distinct NF-kB pathways that lead to either osteoclastogenesis or osteoblastogenesis. The mechanisms according to which NF-κB can induce osteoclastogenesis downstream of receptor activator of nuclear factor-kappa B ligand/receptor activator of nuclear factor-kappa B (RANKL/RANK) are not yet completely understood. According to a recent study by Veeriah et al. [80], the osteoclastogenesis pathway could be described as follows: the pro-inflammatory cytokine IL-1β becomes active upon cleavage by caspase-1 and acts a pro-osteoclastogenic factor [80,81]. Ineffective in osteoblast proliferation, but active in reducing their differentiation, the pleiotropic and acute-phase protein Lipocalin 2 (LCN2) is upregulated by inflammation and its induction produces significant osteoblast impairment. LCN2 in turn stimulates RANKL production by osteoblasts, which favor osteoclastogenesis and bone resorption. Parallel to the IL-1β/LCN2/RANKL pathway, NF-kB activation also induces NOS2, which

increases osteoblast proliferation through the formation of NO molecules that downstream target Cyclooxygenase-2 COX2 (NOS2/NO/COX2 pathway). Maintaining the balance between these two pathways is key for the metabolism of healthy bone. We have shown here that the $Si_3N_4$ surface could become an exogenous NO donor in aqueous solution as a consequence of the homolytic cleavage of its covalent Si-N bonds. NO molecules are generated from ammonia and its subsequent monooxygenase by means of free electrons made available by both silanol dissociation and by partially reduced oxygen radical byproducts that form as a consequence of leakage from transport chains of cytochrome c oxidase enzymatic catalysis in the mitochondrion. Such an amount of exogenously produced NO is expected to boost the NOS2/NO/COX2 pathway and to promote osteoblastogenesis, as seen in Figure 7. In a recent paper, Shen et al. [13,82] found that pH values >8 at the cell–substrate interface greatly enhance both cell proliferation and alkaline phosphatase activity of osteoblasts. This study is important because it shifts the focus in osteogenesis to the chemistry of the solid–liquid interface as a critical factor in bone regeneration. We have previously reported [48,49] that the interfacial pH at the cell/$Si_3N_4$ interface is locally enhanced and stabilized around a value ~8.25. This may be of importance in explaining the enhanced activity of mesenchymal cells on the $Si_3N_4$ surface; alkalosis is known to promote bone formation [83] while systemic acidosis promotes bone resorption [84–86].

In conclusion, the good agreement described in Section 2.2 among Gla/Glu-osteocalcin assays, IGF-1 assay, ALP assay, and quantitative laser microscopy volumetric assessments of bony apatite deposited by cells after 14 days of culture provided proof that cell differentiation into mature osteoblasts, production of osteocalcin binding onto apatite, and successive growth of bony tissue were greatly enhanced when mesenchymal progenitor cells became exposed to $Si_3N_4$ substrates. Moreover, the decreases in tryptophan and phospholipids Raman signals observed in the Raman spectrum of mesenchymal cells exposed to $Si_3N_4$ substrates provide spectroscopic fingerprints of osteoblastogenesis. This interpretation of the *in situ* Raman data is consistent with the outputs of biological assays, as seen in Figure 3, for cells exposed to $Si_3N_4$ substrate. On the basis of our present findings, the $Si_3N_4$ surface chemistry with its interfacial pH buffering effect and friendly RNS kinetics might be exploited in counteracting bone resorption pathologies, in promoting bone repair, and in many related contexts in bone-tissue engineering.

### 3.3. ROS Formation and the Issue of Bone Resorption

The biomedical grade Ti6Al4V alloy substrate tested in this study showed the least cell proliferation rate among the tested substrates, as seen in Figure 2. However, the concentrations of Gla-osteocalcin and IGF-1 supernatants, which characterize the propensity to differentiate into osteoblasts, were slightly higher than that of cells exposed to $Al_2O_3$ substrates, as seen in Figure 3a,c. An explanation for the observed trends could be that, although the metal ions eluted from the surface of the alloy disrupt cell proliferation, the isolated groups of mesenchymal cells that succeed in surviving and differentiating into osteoblasts deposit a protein layer at the solid interface, which eliminates a direct metal/cell interface. This explanation is supported by the "island-like" morphology and the osteopontin-rich composition of bony apatite observed for *in vitro* osteoblast cultures on Ti6Al4V alloy substrates [10,87]. Biocompatibility is generally related with the corrosion property of the metallic alloy and its surface treatments because metal ions can be released into the adjacent environment during the corrosion process affecting the periprosthetic tissues [88–91].

Thompson and Puleo [92] were the first to spot the metal ions released from Ti6Al4V implant components as potentially disturbing agents of the normal functions of bone cells. Such ions stimulate bone resorption by osteoclasts or inhibit bone synthesis by osteoblasts. To prove their hypothesis, these researchers exposed osteogenic cells to metal ions and studied the short-term (48 h) effects of $Ti^{4+}$ and $Al^{3+}$ ions on the osteoblastic phenotype [93]. These pioneering studies determined toxicity of such metal ions, which caused gross cell death. The seriously deleterious effect of $Ti^{4+}$ and $Al^{3+}$ ions on mesenchymal cell cultures at physiologically relevant concentrations was attributed to the interference by these ions with cell differentiation into mature osteoblasts. According to *in vitro* data,

these researchers predicted that the interference of metal ions associated with Ti6Al4V implants with normal osteoblastic differentiation could decrease normal *in vivo* bone deposition and contribute to implant failure by impairing bone repair. This describes the current situation, which is partly observed for Ti6Al4V components of dental implants according to the most recent official statistics [94]. From the point of view of the osteogenic behavior of Ti6Al4V alloys, the present *in vitro* study does not add new data to the published literature. However, we report here a slow rate for mesenchymal cell proliferation and differentiation into osteoblasts, as seen in Figures 2 and 3a,c, accompanied by a clear propensity to differentiate into osteoclasts, as seen in the Glu-osteocalcin data in Figure 3b. Moreover, the volumetric amount of bony apatite produced in 14 days by the present cell culture on $Al_2O_3$ substrates was the least among the tested substrates, as seen in Figure 3d. $Al_2O_3$ is not cytotoxic to human cells and is generally considered as a fully bioinert biomaterial [1–3], which may be a fair statement when this oxide bioceramic is compared with metallic materials. However, the present study clarifies that the $Al_2O_3$ surface does not represent a friendly environment for mesenchymal cells. In addition, we explain the poor outputs of $Al_2O_3$ in osteogenic performance as a consequence of its non-bioinert surface chemistry, as seen in Figure 6e,f. A dehydroxylation reaction leading to the formation ROS, including hydroxyl, and liberated $Al^{3+}$ ions in aqueous solution might induce lipid rigidification/peroxidation, delay osteoblastogenesis, and inhibit the effect of mineralization. We have also put forward spectroscopic proofs for a propensity to apoptosis for mesenchymal cells exposed to $Al_2O_3$ substrates, which was comparable with that of cells exposed to those of Ti6Al4V, as seen in Figure 5c,d. The decrease in DNA Raman bands and the increase in bands related to lipids, described in Section 2.3, are fingerprints of incipient apoptosis induced by ROS and metal ions (as generated in different concentrations) on Ti6Al4V alloy and $Al_2O_3$ substrates. The kinetics of dehydroxylation and ionic elution from the $Al_2O_3$ surface might be quite slow under static conditions at physiological pH. However, the ionic elution kinetics could significantly be accelerated under frictional conditions or in an acidic environment. In view of its poor osteogenic performance and because of the above reasons, components made of $Al_2O_3$ bioceramics might not be suitable for implants subjected to friction or highly localized stresses in the human body; they may also be prone to infections. Accordingly, we believe that $Si_3N_4$ non-oxide bioceramics are more suitable than oxide bioceramics, despite a number of publications have suggested the use of $Al_2O_3$ and $Al_2O_3$-based biomaterials as components for dental and spinal fusion implants [95–99]. Components for these biomedical applications, which require a quick, massive, and long-term protracted osteogenesis, should be designed not only in consideration of the structural reliability of the bioceramic [100] but also of their short- and long-term osteogenic attitudes.

## 3.4. Possible New Applications and the Future of $Si_3N_4$ Bioceramics

The focus of the present study was to present a detailed explanation of the physical chemistry circumstances behind the friendly interaction and kinetics of $Si_3N_4$ toward osteoblasts. In particular, we targeted the positive contribution of this non-oxide material as an exogenous NO donor in osteoblastogenesis. On the one hand, this finding clearly strengthens the suitability of $Si_3N_4$ bioceramic in spine arthrodesis, which is currently its primary application as a biomedical component. On the other hand, it also paves the way to establish new biomedical applications for this material, in which the balance between osteoblast and osteoclast activity, which governs bone turnover, needs to be restored. For example, $Si_3N_4$ could be used as bulk components in various arthroplastic applications (also in view of its excellent mechanical properties [100]) or as a coating to metallic stems and acetabular components of hip joints to limit any long-term contact between metal surfaces and bone tissue. The use of $Si_3N_4$ components could be particularly useful in primary surgeries on patients affected by osteoporosis or for those patients for whom the primary surgery has produced osteolytic bones. The paradigmatic shift in surgeries based on the $Si_3N_4$ approach would thus potentially consist of using a "therapeutic" rather than a passively inert biomaterial for artificial implants. Exploiting the long-term supportive (chemical) driving force and the friendly kinetics of $Si_3N_4$ bioceramics will

not only elongate the in-service lifetime of implanted components but also restore the fundamental function of osteoblastogenesis in patients affected by osteoporosis or by other degenerative changes associated with aging. In this context, the availability of a "therapeutic" (rather than inert) biomaterial with long-term kinetics efficacy such as $Si_3N_4$ could represent an important option in societies with an increasing elderly population.

## 4. Materials and Methods

### 4.1. X-ray Photoelectron Spectroscopy

Dense Ø12.7 mm × 1 mm and finely polished discs of silicon nitride ($Si_3N_4$, $Mc^{2®}$, SINTX Corporation, Salt Lake City, UT, USA), titanium alloy (Ti6Al4V, ASTM F136), and medical grade alumina ($Al_2O_3$, BIOLOX®Forte, CeramTec GmbH, Plochingen, Germany) were prepared. XPS experiments were then carried out on the surfaces of the different substrates to characterize their surface chemistry before and after exposure to aqueous environment at neutral pH. To accelerate the reactions, the samples were exposed to water vapor environment at 121 °C up to 48 h. XPS data were then collected with a photoelectron spectrometer (JPS-9010 MC; JEOL Ltd., Tokyo, Japan) equipped with an X-ray source of monochromatic $MgK_\alpha$ (10 kV, 10 mA). The vacuum in the chamber was set at $2 \times 10^{-7}$ Pa, with analyzer pass energy at 10 eV and voltage step size at 0.1 eV. X-ray angle of incidence and takeoff angle were 34° and 90°, respectively. The XPS tests were validated at $n = 6$ for $Si_3N_4$ and Ti6Al4V alloy substrates, and at $n = 8$ for the $Al_2O_3$ substrate.

### 4.2. Cell Culture

KUSA-A1 mesenchymal bone marrow stromal stem cells (JCRB Cell Bank, Osaka, Japan) were cultured in a medium containing 4.5 g/L of glucose DMEM (D-glucose, L-glutamine, phenol red, and sodium pyruvate) supplemented with 10% fetal bovine serum. Cells were set on Petri dishes for 24 h at 37 °C.

### 4.3. Cell Proliferation and Metabolism

Disks of different materials were ultrasonically cleaned and UV-sterilized prior to being seeded with $1 \times 10^5$/mL KUSA-A1 cells. They were then seeded with placing them into well plates in an osteogenic media (Dulbecco's modified Eagle medium (DMEM) and 10 wt.% fetal bovine serum, ascorbic acid, hydrocortisone, and β-Glycerophosphate. This medium was refreshed twice weekly during a total of 14 days incubation period. Seeding of KUSA-A1 cells into empty well plates (made of silica glass) with and without the osteogenic medium served as positive and negative controls, respectively. The silica glass substrate was assumed to be completely inert toward cell metabolism and the cell response on it was only regulated by the presence or absence of osteogenic medium.

To monitor short-term proliferation, the cells were stained for fluorescence microscopy with Alexa Fluor® 488 Phalloidin Thermo Fisher Scientific, Waltham, MA, USA) and Hoechst 33342 (Dojindo, Kumamoto, Japan) for 1 h. They were then washed three times with 1 mL TBST solution (mixture of Tris-Buffered Saline and Tween 20). Fluorescence spectroscopy images for cell counting were taken at 24 h with a fluorescence microscope of the type BZ-X700 (Keyence, Osaka, Japan). The number of cells per unit area was directly counted on fluorescence micrographs (total area of ~1 mm² for each time and type of substrate). The results of cell counting were validated at $n = 4$ for each investigated substrate.

Some of the seeded discs for each type of material were also subjected to *in situ* laser Raman microscopy inspections (Raman-touch, Nanophoton, Osaka, Japan) to obtain information about the metabolism and the state of differentiation of the mesenchymal progenitor cells after very short-term (48 h) exposure to the respective substrates.

### 4.4. Bony Apatite Formation

After 14 days of culture on different substrates, a 3D laser-scanning microscope with a 150× objective lens at a numerical aperture of 0.9 (VK-X200, K series, Keyence, Osaka, Japan) was utilized to determine the volume of bony apatite formed on the biomaterial substrates. The volumetric amounts of bony tissue deposited by the cells per unit area was calculated from line scan profiles over the entire substrate using automatic software provided by the maker of the 3D laser-scanning microscope. The tests were validated at $n = 6$ for each investigated substrate.

### 4.5. IGF-1 Measurement

IGF-1 signaling was used as a probe for measuring cell proliferation and differentiation efficiency. IGF-1 is a protein that stimulates both differentiation and apatite growth. It has been reported to be a main modulator for bone growth through endocrine/paracrine and autocrine mechanisms [11,74]. We employed the mouse IGF-1 ELISA (R&D Systems, Minneapolis, MN, USA) to measure IGF-1 concentration in the KUSA-A1 cell culture supernatants. Samples were first incubated for 1 h at room temperature, 0.1 mL of streptavidin solution was added, and the samples were incubated for 45 min at room temperature. Further addition of 0.1 mL of TMB one-step substrate reagent was made and, after incubation for 30 min at room temperature, 0.05 mL of stop solution was added. Optical densities at 450 nm were measured immediately after these procedures. The tests were validated at $n = 4$ for each investigated substrate.

### 4.6. Gla/Glu Osteocalcin Measurement

The Mouse Gla-Osteocalcin High Sensitive EIA Kit (Cat. #MK127; Takara Bio, Inc., Kusatsu, Shiga Prefecture, Japan) revealed Gla-type osteocalcin by means of a monoclonal antibody included in the used kit. Mouse Glu-Osteocalcin High Sensitive EIA Kit (Cat. #MK129; Takara Bio, Inc., Kusatsu, Shiga Prefecture, Japan) directly assessed decarboxylated osteocalcin from synthesized tissue by measuring enzymes peculiar to osteoclasts as well as the inactive (Glu-type) osteocalcin that they produce. Glu/Gla-osteocalcin EIA Kits could be directly used with cell-culture media containing fetal bovine serum because they did not cross-react with bovine antigens. These assays were applied according to manufacturer's recommendations. Briefly, the Kit's reagents (0.1 mL each) and the samples were made ready in separate well plates and then added to the Antibody Coated Microtiter plate at room temperature for 1 h. The reaction mixture was subsequently cast aside and the samples rinsed three times with 0.1% wash buffer (Tween 20/PBS). Successively, 0.1 mL of peroxidase (POD)-labeled Antibody Solution was poured in the wells with an 8-channel pipette and made reacting for 1 h at room temperature. The reaction mixture was set aside by washing four times with 0.1% wash Tween 20/PBS, 0.1 mL of Substrate Solution (TMBZ) at room temperature for 15 min. A highly viscous stop solution in a quantity of 0.1 mL was mixed into each well and kept for 1 h until formation of a stable color. Absorbance was then measured at 450 nm (zero value on distilled water) and plots constructed of concentration values of Gla/Glu-osteocalcin. Cells cultured on silica glass with and without the osteogenic medium were taken as positive and negative control samples, respectively. The experimental conditions adopted for these latter samples were the same as those applied to cells exposed to the tested substrates. Accordingly, we assumed that the silica glass substrate was completely inert toward cell metabolism and that, for the control silica glass substrate, the cell response was only regulated by presence or absence of osteogenic medium. The Gla/Glu-osteocalcin tests were validated at $n = 4$ for each investigated substrate.

### 4.7. ALP Stain Assay

The membrane-bound enzyme ALP, a marker of osteogenic differentiation, was measured on KUSA-A1 cells exposed to different substrates for nine days in osteogenic medium. The ALP activity was monitored upon staining with the TRAP/ALP Stain Kit (Wako, Osaka, Japan), according

to the manufacturer's instructions. ALP activity was assessed through direct pixel counting on optical micrographs.

*4.8. Statistics*

The elemental fractions of bonds detected by XPS on the surface of different surfaces, the number of cells per unit area, the concentrations of Glu/Gla-osteocalcin and IGF-1, and the volumetric amounts of bony tissue deposited by the cells per unit area were expressed as mean values ± one standard deviation. The results were statistically compared using one-way Analysis of Variance (ANOVA) on a sampling population, $n = 4$. A value of $p < 0.003$ was considered statistically significant and labeled with two asterisks.

## 5. Conclusions

The main conclusions of this paper can be summarized as follows:

(i) $Si_3N_4$ bioceramics presented osteoinductive properties by virtue of their peculiar surface chemistry, which evolved at the biomolecular interface with cell-friendly kinetics. The homolytic cleavage of Si-N bonds at the solid surface triggered a cascade of chemical reactions that could locally uplift pH and produce RNS (specifically NO) in low concentrations lying in the range of signaling used by cells in osteoblastogenesis crosstalk.

(ii) Neither Ti6Al4V alloy nor $Al_2O_3$ bioceramic substrates could be recognized to trigger osteoinductivity with respect to mesenchymal KUSA-A1 progenitor cells. Unlike the RNS involved with the $Si_3N_4$ surface chemistry, the ionic elution of metal species and the ROS involved with the surface chemistry of these two latter biomaterials were similarly detrimental to cell proliferation, their differentiation, and osteogenesis. Although not cytotoxic according to standard definitions of cytotoxicity, both these widely used biomaterials induced an apoptotic tendency in mesenchymal progenitor cells.

(iii) The present data partly answered a number of concerns raised by the statistics recently published by the National Consumer Affairs Center of Japan (and successively recognized by The Japanese Society of Oral Implantology) regarding malfunctioning of dental implants [94]. We believe that the origin of medium/long-term failures of dental implants is partly related to their adverse chemical interactions with the periprosthetic tissue in overlap with the severe environmental and mechanical stress conditions of the oral cavity.

(iv) The friendly exogenous NO kinetics of $Si_3N_4$ bioceramics could be further exploited in counteracting bone resorption pathologies and in promoting bone repair.

**Author Contributions:** G.P., B.J.M. and B.S.B. conceived and planned the experiments. M.Z. prepared the samples and carried out the experiments together with F.B. and T.A., under the supervision and with the contribution of E.M. and W.Z., who also contributed to the interpretation of the results. G.P. took the lead in writing the manuscript, which was further edited by B.S.B. and B.J.M. M.Z., F.B., T.A., E.M. and W.Z. also contributed the final version of the manuscript. All authors provided critical feedback and helped shaping research, analyses and manuscript text.

## References

1. Hench, L.L. Bioceramics: From concept to clinic. *J. Am. Ceram. Soc.* **1991**, *74*, 1487–1510. [CrossRef]
2. Salinas, A.J.; Esbrit, P.; Vallet-Regi, M. A tissue engineering approach based on the use of bioceramics for bone repair. *Biomater. Sci.* **2013**, *1*, 40–51. [CrossRef]
3. Piconi, C. Bioinert ceramics: State-of-the-art. *Key Eng. Mater.* **2017**, *758*, 3–13. [CrossRef]
4. Yuan, H.; Yang, Z.; Li, Y.; Zhang, X.; De Bruijn, J.D.; De Groot, K. Osteoinduction by calcium phosphate biomaterials. *J. Mater. Sci. Mater. Med.* **1998**, *9*, 723–726. [CrossRef] [PubMed]
5. Fellah, B.H.; Gauthier, O.; Weiss, P.; Chappard, D.; Layrolle, P. Osteogenicity of biphasic calcium phosphate ceramics and bone autograft in a goat model. *Biomaterials* **2008**, *29*, 1177–1188. [CrossRef]
6. Yuan, H.; de Bruijn, J.D.; Zhang, X.; van Blitterswijk, C.A.; de Groot, K. Osteoinduction by porous alumina ceramic. In Proceedings of the 16th European Conference on Biomaterials, London, UK, 9–12 September 2001; p. 209.
7. Fujibayashi, S.; Neo, M.; Kim, H.M.; Kokubo, T.; Nakamura, T. Osteoinduction of porous bioactive titanium metal. *Biomaterials* **2004**, *25*, 443–450. [CrossRef]
8. Takemoto, M.; Fujibayashi, S.; Matsushita, T.; Suzuki, J.; Kokubo, T.; Nakamura, T. Osteoinductive ability of porous titanium implants following three types of surface treatment. In Proceedings of the 51st Ann Meet Orthop Res Soc, Washington DC, USA, 20–23 February 2005. poster 0992.
9. Webster, T.J.; Patel, A.A.; Rahaman, M.N.; Bal, B.S. Anti-infective and osteointegration properties of silicon nitride, poly(ether ether ketone), and titanium implants. *Acta Biomater.* **2012**, *8*, 4447–4454. [CrossRef] [PubMed]
10. Pezzotti, G. Silicon nitride: A bioceramic with a gift. *ACS Appl. Mater. Interfaces* **2019**. [CrossRef] [PubMed]
11. Lee, W.-C.; Guntur, A.R.; Long, F.; Rosen, C.J. Energy metabolism of the osteoblast: Implication for osteoporosis. *Endocrine Rev.* **2017**, *38*, 255–266. [CrossRef] [PubMed]
12. Nichols, F.C.; Neuman, W.F. Lactic acid production in mouse calvaria in vitro with and without parathyroid hormone simulation: Lack of acetazolamide effects. *Bone* **1987**, *8*, 105–109. [CrossRef]
13. Shen, Y.; Liu, W.; Lin, K.; Pan, H.; Darvell, B.W.; Peng, S.; Wen, C.; Deng, L.; Lu, W.W.; Chang, J. Interfacial pH: A critical factor for osteoporotic bone regeneration. *Langmuir* **2011**, *27*, 2701–2708. [CrossRef] [PubMed]
14. Lin, K.; Xia, L.; Li, H.; Jiang, X.; Pan, H.; Xu, Y.; Lu, W.W.; Zhang, Z.; Chang, J. Enhanced osteoporotic bone regeneration by strontium-substituted calcium silicate bioactive ceramics. *Biomaterials* **2013**, *34*, 10028–10042. [CrossRef] [PubMed]
15. Naumkin, A.V.; Kraut-Vass, A.; Gaarenstroom, S.W.; Powell, C.J. NIST *X-Ray Photoelectron Spectroscopy Database*; NIST Standard Reference Database 20, Version 4.1. Nat'l Std. Ref. Data Series (NIST NSRDS); National Institute of Standards and Technology: Gaithersburg, MD, USA, 2012. Available online: https: //srdata.nist.gov/xps/ (accessed on 21 August 2019).
16. Healy, K.E.; Ducheyne, P. The mechanism of passive dissolution of titanium in a model physiological environment. *J. Biomed. Mater. Res.* **1992**, *26*, 319–338. [CrossRef] [PubMed]
17. Healy, K.E.; Ducheyne, P. Hydration and preferential molecular adsorption on titanium in vitro. *Biomaterials* **1992**, *13*, 553–561. [CrossRef]
18. Hierro-Oliva, M.; Gallardo-Moreno, A.M.; Gonzales-Martin, M.L. XPS analysis of Ti6Al4V oxidation under UHV conditions. *Metall Mater. Trans. A* **2014**, *45A*, 6285–6290. [CrossRef]
19. Böhm, H.P. Acidic and basic properties of hydroxylated metal oxide surfaces. *Discuss Faraday Soc.* **1971**, *52*, 264–275. [CrossRef]
20. Carbonio, E.A.; Rocha, T.C.R.; Klyushin, A.Y.; Pis, I.; Magnano, E.; Nappini, S.; Piccinin, S.; Knop-Gericke, A.; Schlögl, R.; Jones, T.E. Are multiple oxygen species selective in ethylene epoxidation on silver? *Chem. Sci.* **2018**, *9*, 990–998. [CrossRef] [PubMed]
21. Grant, R.B.; Lambert, R.M. Ethylene oxide isomerisation on single-crystal Ag(111) in atomically clean and Cs-moderated conditions. *J. Catal.* **1985**, *93*, 92–99. [CrossRef]
22. Grant, R.B.; Lambert, R.M. Alkali metal promoters and catalysis: A single-crystal investigation of ethylene epoxidation on Cs-doped Ag(lll). *Langmuir* **1985**, *1*, 29–33. [CrossRef]
23. Zambelli, T.; Barth, J.V.; Wintterlin, J. Thermal dissociation of chemisorbed oxygen molecules on Ag(110): An investigation by scanning tunneling microscopy. *J. Phys.* **2002**, *14*, 4241–4250. [CrossRef]
24. Gaigeot, M.-P.; Sprik, M.; Sulpizi, M. Oxide/water Interfaces: How the surface chemistry modifies interfacial water properties. *J. Phys. Condens. Matter.* **2012**, *24*, 124106. [CrossRef] [PubMed]

25. Notingher, I.; Bisson, I.; Polak, J.M.; Hench, L.L. In situ spectroscopic study of nucleic acids in differentiating embryonic stem cells. *Vib. Spectrosc.* **2004**, *35*, 199–203. [CrossRef]

26. Movasaghi, Z.; Rehman, S.; Rehman, I.U. Raman spectroscopy of biological tissues. *Appl. Spectrosc. Rev.* **2007**, *42*, 493–541. [CrossRef]

27. Madzharova, F.; Heiner, Z.; Guehlke, M.; Kneipp, J. Surface-enhanced hyper-Raman spectra of adenine, guanine, cytosine, thymine, and uracil. *J. Phys. Chem.* **2016**, *120*, 15415–15423. [CrossRef]

28. Notingher, I.; Bisson, I.; Bishop, A.E.; Randle, W.L.; Polak, J.M.P.; Hench, L.L. In situ spectral monitoring of mRNA translation in embryonic stem cells during differentiation in vitro. *Anal. Chem.* **2004**, *76*, 3185–3193. [CrossRef] [PubMed]

29. Lopes, R.P.; Marques, M.P.M.; Valero, R.; Tomkinson, J.; Batista De Carvalho, L.A.E. Guanine-A combined study using vibrational spectroscopy and theoretical methods. *Spectrosc. Int.* **2012**, *27*, 273–292. [CrossRef]

30. Krafft, C.; Neudert, L.; Simat, T.; Salzer, R. Near infrared Raman spectra of human brain lipids. *Spectrochim. Acta A Mol. Biomol. Spectrosc.* **2005**, *61*, 1529–1535. [CrossRef]

31. Rimai, L.; Cole, T.; Parsons, J.L.; Hickmott, J.T.; Carew, E.B. Studies of Raman spectra of water solutions of adenosine tri-, di-, and monophosphate and some related compounds. *Biophys. J.* **1969**, *9*, 320–329. [CrossRef]

32. Bhaumik, A.; Shearin, A.M.; Delong, R.; Wanekaya, A.; Ghosh, K. Probing the interaction at the nano-bio interface using Raman spectroscopy: ZnO particles and adenosine triphosphate biomolecules. *J. Phys. Chem. C* **2014**, *118*, 18631–18639. [CrossRef]

33. Radi, R. Nitric oxide, oxidants, and protein tyrosine nitration. *Proc. Natl. Acad. Sci. USA* **2004**, *101*, 4003–4008. [CrossRef]

34. Vidal, C.; Li, W.; Santner-Nanan, B.; Lim, C.K.; Guillemin, G.J.; Ball, H.J.; Hunt, N.H.; Nanan, R.; Duque, G. The kynurenine pathway of tryptophan degradation is activated during osteoblastogenesis. *Stem Cells* **2015**, *33*, 111–121. [CrossRef] [PubMed]

35. El Refaey, M.; McGee-Lawrence, M.E.; Fulzele, S.; Kennedy, E.J.; Bollag, W.B.; Elsalanty, M.; Zhong, Q.; Ding, K.-H.; Bendzunas, N.G.; Shi, X.-M.; et al. Kynurenine, a tryptophan metabolite that accumulates with age, induces bone loss. *J. Bone Miner. Res.* **2017**, *32*, 2182–2193. [CrossRef]

36. Michalowska, M.; Znorko, B.; Kaminski, T.; Oksztulska-Kolanek, E.; Pawlak, D. New insights into tryptophan and its metabolites in the regulation of bone metabolism. *J. Physiol. Pharmacol.* **2015**, *66*, 779–791.

37. Martin-Molina, A.; Rodrigues-Beas, C.; Farando, J. Effect of calcium and magnesium on phosphatidylserine membranes: Experiments and all-atomic simulations. *Biophys. J.* **2012**, *102*, 2095–2103. [CrossRef] [PubMed]

38. Brauchle, E.; Thude, S.; Bruker, S.Y.; Schenke-Layland, K. Cell death stages in single apoptotic and necrotic cells monitored by Raman microspectroscopy. *Sci. Rep.* **2014**, *4*, 4698. [CrossRef] [PubMed]

39. Notingher, I.; Green, C.; Dyer, C.; Perkins, E.; Hopkins, N.; Lindsay, C.; Hench, L.L. Discrimination between ricin and sulphur mustard toxicity in vitro using Raman spectroscopy. *J. R. Soc. Interface* **2004**, *1*, 79–90. [CrossRef]

40. Redza-Dutordoir, M.; Averill-Bates, D.A. Activation of apoptosis signaling pathways by reactive oxygen species. *Biochim. Biophys. Acta Mol. Cell Res.* **2016**, *1863*, 2977–2992. [CrossRef]

41. Kajdas, C. General approach to mechanochemistry and its relation to tribochemistry. In *Tribology in Engineering*; Pihtili, H., Ed.; InTech: London, UK, 2013; pp. 209–240.

42. Mezzasalma, S.; Baldovino, D. Characterization of silicon nitride surface in water and acid environment: A general approach to the colloidal suspensions. *J. Colloid Interface Sci.* **1996**, *180*, 413–420. [CrossRef]

43. Sonnefeld, J. Determination of surface charge density parameters of silicon nitride. *Colloids Surf. A* **1996**, *108*, 27–31. [CrossRef]

44. Pezzotti, G.; Marin, E.; Adachi, T.; Rondinella, A.; Boschetto, F.; Zhu, W.; Sugano, N.; Bock, R.M.; McEntire, B.; Bal, B.S. Bioactive silicon nitride: A new therapeutic material for osteoarthropathy. *Sci. Rep.* **2017**, *7*, 44848. [CrossRef] [PubMed]

45. Vatansever, F.; de Melo, W.C.M.A.; Avci, P.; Vecchio, D.; Sadasivam, M.; Gupta, A.; Chandran, R.; Karimi, M.; Parizotto, N.A.; Yin, R.; et al. Antimicrobial strategies centered around reactive oxygen species - bactericidal antibiotics, photodynamic therapy, and beyond. *FEMS Microbiol. Rev.* **2013**, *37*, 955–989. [CrossRef] [PubMed]

46. Stein, L.Y.; Yung, Y.L. Production, isotopic composition, and atmospheric fate of biologically produced nitrous oxide. *Annu Rev. Earth Planet Sci.* **2003**, *31*, 329–356. [CrossRef]

47. Schneider, M.; Marison, I.W.; von Stockar, U. The importance of ammonia in mammalian cell culture. *J. Biotechnol.* **1996**, *46*, 161–185. [CrossRef]

48. Pezzotti, G.; Bock, R.M.; McEntire, B.J.; Jones, E.; Boffelli, M.; Zhu, W.; Baggio, G.; Boschetto, F.; Puppulin, L.; Adachi, T.; et al. Silicon nitride bioceramics induce chemically driven lysis in Porphyromonas gingivalis. *Langmuir* **2016**, *32*, 3024–3035. [CrossRef] [PubMed]

49. Pezzotti, G.; Bock, R.M.; McEntire, B.J.; Adachi, T.; Marin, E.; Boschetto, F.; Zhu, W.; Mazda, O.; Bal, S.B. In vitro antibacterial activity of oxide and non-oxide bioceramics for arthroplastic devices: I. In situ time-lapse Raman spectroscopy. *Analyst* **2018**, *143*, 3708–3721. [CrossRef] [PubMed]

50. Jennison, T.; McNally, M.; Pandit, H. Review - prevention of infection in external fixation pin sites. *Acta Mater.* **2014**, *10*, 595–603.

51. Dong, H.; Mukinay, T.; Li, M.; Hood, R.; Soo, S.L.; Cockshott, S.; Sammons, R.; Li, X. Improving tribological and anti-bacterial properties of titanium external fixation pins through surface ceramic conversion. *J. Mater. Sci.* **2017**, *28*, 5. [CrossRef]

52. Page, K.; Wilson, M.; Parkin, I.P. Antimicrobial surfaces and their potential in reducing the role of the inanimate environment in the incidence of hospital- acquired infections. *J. Mater. Chem.* **2009**, *19*, 3818–3831. [CrossRef]

53. Fujishima, A.; Hashimoto, K.; Watanabe, T. *TiO$_2$ Photocatalysis*; Bkc Inc. Pub. Co.: Tokyo, Japan, 2000.

54. Mills, A.; Lee, S. A web-based overview of semiconductor photochemistry-based current commercial applications. *J. Photochem. Photobiol. Chem.* **2002**, *152*, 233–247. [CrossRef]

55. Kiwi, J.; Rtimi, S.; Sanjines, R.; Pulgarin, C. TiO$_2$ and TiO$_2$-doped films able to kill bacteria by contact: New evidence for the dynamics of bacterial inactivation in the dark and under light irradiation. *Int. J. Photoenergy* **2014**, 785037. [CrossRef]

56. Zubkoy, T.; Stahl, D.; Thompson, T.L.; Panayotov, D.; Diwald, O.; Yates, J.T., Jr. Ultraviolet light-induced hydrophilicity effect on TiO$_2$(110) (1x1). Dominant role of the photooxidation of adsorbed hydrocarbons causing wetting by water droplets. *J. Phys. Chem. B* **2005**, *109*, 15454–15462. [CrossRef] [PubMed]

57. Wang, R.; Hashimoto, K.; Fujishima, A.; Chikuni, M.; Kojima, E.; Kitamura, A.; Shimohigoshi, M.; Watanabe, T. Light-induced amphiphilic surfaces. *Nature* **1997**, *388*, 431–432. [CrossRef]

58. Kadam, S.; Shai, S.; Shahane, A.; Kaushik, K.S. Recent advances in non-conventional antimicrobial approaches for chronic wound biofilms: have we found the 'chink in the armor'? *Biomedicines* **2019**, *7*, 35. [CrossRef]

59. Shapovalov, V.; Truong, T.N. Ab Initio study of water adsorption on α- Al$_2$O$_3$ (0001) crystal surface. *J. Phys. Chem. B* **2000**, *104*, 9859–9863. [CrossRef]

60. Fernández, E.M.; Eglitis, R.I.; Borstel, G.; Balbás, L.C. Ab initio calculations of H$_2$O and O$_2$ adsorption on Al$_2$O$_3$ substrates. *Comput. Mater. Sci.* **2007**, *39*, 587–592. [CrossRef]

61. Lu, Y.-H.; Chen, H.-T. Hydrogen generation by the reaction of H$_2$O with Al$_2$O$_3$-based materials: A computational analysis. *Phys. Chem. Chem. Phys.* **2015**, *17*, 6834–6843. [CrossRef]

62. Blumenthal, N.C.; Posner, A.S. In vitro model of aluminum-induced osteomalacia: Inhibition of hydroxyapatite formation and growth. *Calcif. Tissue Int.* **1984**, *36*, 439–441. [CrossRef] [PubMed]

63. Campbell, A.; Becaria, A.; Lahiri, D.K.; Sharman, K.; Bondy, S.C. Chronic exposure to aluminum in drinking water increases inflammatory parameters selectively in the brain. *J. Neurosci. Res.* **2004**, *75*, 565–572. [CrossRef]

64. Chambers, J.W.; LoGrasso, P.V. Mitochondrial c-Jun N-terminal kinase (JNK) signaling initiates physiological changes resulting in amplification of reactive oxygen species generation. *J. Biol. Chem.* **2011**, *286*, 16052–16062. [CrossRef]

65. Tournier, C.; Hess, P.; Yang, D.D.; Xu, J.; Turner, T.K.; Nimnual, A.; Bar-Sagi, D.; Jones, S.N.; Flavell, R.A.; Davis, R.J. Requirement of JNK for stress-induced activation of the cytochrome c-mediated death pathway. *Science* **2000**, *288*, 870–874. [CrossRef]

66. Li, X.; Han, Y.; Guan, Y.; Zhang, L.; Bai, C.; Li, Y. Aluminum induces osteoblast apoptosis through the oxidative stress-mediated JNK signaling pathway. *Biol. Trace Elem. Res.* **2012**, *150*, 502–508. [CrossRef] [PubMed]

67. Wimalawansa, S.J. Nitric oxide: Novel therapy for osteoporosis. *Expert Opin. Pharmacother.* **2018**, *9*, 3025–3044. [CrossRef] [PubMed]

68. Feelisch, M. The use of nitric oxide donors in pharmacological studies. *Naunyn Schmiedeberg's Arch. Pharmacol.* **1998**, *358*, 113–122. [CrossRef]

69. Felka, T.; Ulrich, C.; Rolauffs, B.; Mittag, F.; Kluba, T.; DeZwart, P.; Ochs, G.; Bonin, M.; Nieselt, K.; Hart, M.L.; et al. Nitric oxide activates signaling by c- Raf, MEK, p-JNK, p38 MAPK and p53 in human mesenchymal stromal cells and inhibits their osteogenic differentiation by blocking expression of Runx2. *J. Stem Cell Res. Ther.* **2014**, *4*, 195.

70.  Abnosi, M.H.; Pari, S. Exogenous nitric oxide induced early mineralization in rat bone marrow mesenchymal stem cells via activation of alkaline phosphatase. *Iranian Biomed. J.* **2019**, *23*, 142–152.

71.  Lockwood, A.; Patka, J.; Rabinovich, M.; Wyatt, K.; Abraham, P. Sodium nitroprusside-associated cyanide toxicity in adult patients-fact or fiction. *J. Clin. Trials* **2010**, *2*, 133–148.

72.  Huitema, L.F.; van Weeren, P.R.; Barneveld, A.; van de Lest, C.H.A.; Helms, J.B.; Vaandrager, A.B. Iron ions derived from the nitric oxide donor sodium nitroprusside inhibit mineralization. *Eur. J. Pharmacol.* **2006**, *542*, 48–53. [CrossRef]

73.  Rauhala, P.; Khaldi, A.; Mohanakumar, K.P.; Chiueh, C.C. Apparent role of hydroxyl radicals in oxidative brain injury induced by sodium nitroprusside. *Free Radic. Biol. Med.* **1998**, *24*, 1065–1073. [CrossRef]

74.  Guntur, A.R.; Le, P.T.; Farber, C.R.; Rosen, C.J. Bioenergetics during calvarial osteoblast differentiation reflect strain differences in bone mass. *Endocrinology* **2014**, *155*, 1589–1595. [CrossRef]

75.  Golub, E.E.; Boesze-Battaglia, K. The role of alkaline phosphatase in mineralization. *Curr. Opin. Orthop.* **2007**, *18*, 444–448. [CrossRef]

76.  Henstock, J.R.; Canham, L.T.; Anderson, S.I. Silicon: The evolution of its use in biomaterials. *Acta Biomater.* **2015**, *11*, 17–26. [CrossRef] [PubMed]

77.  Shie, M.-Y.; Ding, S.-J.; Chang, H.-C. The role of silicon in osteoblast-like cell proliferation and apoptosis. *Acta Biomater.* **2011**, *7*, 2604–2614. [CrossRef]

78.  Pezzotti, G.; Oba, N.; Zhu, W.; Marin, E.; Rondinella, A.; Boschetto, F.; McEntire, B.; Yamamoto, K.; Bal, B.S. Human osteoblasts grow transitional Si/N apatite in quickly osseointegrated $Si_3N_4$ cervical insert. *Acta Biomat.* **2017**, *64*, 411–420. [CrossRef] [PubMed]

79.  Boyce, B.F.; Yao, Z.; Xing, L. Functions of NF-kB in bone. *Ann N. Y. Acad. Sci.* **2010**, *1192*, 367–375. [CrossRef]

80.  Veeriah, V.; Zanniti, A.; Paone, R.; Chatterjee, S.; Rucci, N.; Teti, A.; Capulli, M. Interleukin-1β, lipocalin 2 and nitric oxide synthase 2 are mechanoresponsive mediators of mouse and human endothelial cell-osteoblast crosstalk. *Sci. Rep.* **2016**, *6*, 29889. [CrossRef] [PubMed]

81.  Nakamura, I.; Jimi, E. Regulation of osteoclast differentiation and function by interleukin-1. *Vitam. Horm.* **2006**, *74*, 357–370.

82.  Shen, Y.; Liu, W.; Lin, K.; Wen, C.; Pan, H.; Wang, T.; Darvell, B.W.; Lu, W.W.; Huang, W. Bone regeneration: importance of local pH – strontium-doped borosilicate scaffold. *J. Mater. Chem.* **2012**, *17*, 8662–8670. [CrossRef]

83.  Bushinsky, D.A. Acid-base imbalance and the skeleton. *Eur. J. Nutr.* **2001**, *40*, 238–244. [CrossRef] [PubMed]

84.  Bushinsky, D.A. Metabolic alkalosis decreases bone calcium efflux by suppressing osteoclasts and stimulating osteoblasts. *Am. J. Physiol.* **1996**, *40*, F216–F222. [CrossRef]

85.  Buclin, T.; Cosma, M.; Appenzeller, M.; Jacquet, A.F.; Decosterd, L.A.; Biollaz, J.; Burckhardt, P. Diet acids and alkalis influence calcium retention in bone. *Osteoporosis Int.* **2001**, *12*, 493–499. [CrossRef] [PubMed]

86.  Arnett, T. Regulation of bone cell function by acid-base balance. *Proc. Nutr. Soc.* **2003**, *62*, 511–520. [CrossRef] [PubMed]

87.  Pezzotti, G.; McEntire, B.J.; Bock, R.; Boffelli, M.; Zhu, W.; Vitale, E.; Puppulin, L.; Adachi, T.; Yamamoto, T.; Kanamura, N.; et al. Silicon nitride: A synthetic mineral for vertebrate biology. *Sci. Rep.* **2016**, *6*, 31717. [CrossRef] [PubMed]

88.  Okazaki, Y.; Rao, S.; Ito, Y.; Tateishi, T. Corrosion resistance, mechanical properties, corrosion fatigue strength and cytocompatibility of new Ti alloys without Al and V. *Biomaterials* **1998**, *19*, 1197–1215. [CrossRef]

89.  Jorge, J.R.; Barão, V.A.; Delben, J.A.; Faverani, L.P.; Queiroz, T.P.; Assunção, W.G. Titanium in dentistry: Historical development, state of the art and future perspectives. *J. Indian Prosthodont Soc.* **2013**, *13*, 71–77. [CrossRef] [PubMed]

90.  Paschoal, A.L.; Vanâncio, E.C.; Canale Lde, C.; da Silva, O.L.; Huerta-Vilca, D.; Motheo Ade, J. Metallic Biomaterials TiN-coated: Corrosion analysis and biocompatibility. *Artif. Organs* **2003**, *27*, 461–464. [CrossRef] [PubMed]

91.  Savadi, R.C.; Goyal, C. Study of biomechanics of porous coated root form implant using overdenture attachment: A 3D FEA. *J. Indian Prosthodont. Soc.* **2010**, *10*, 168–175. [CrossRef] [PubMed]

92.  Thompson, G.J.; Puleo, D.A. Ti-6Al-4V ion solution inhibition of osteogenic cell phenotype as a function of differentiation timecourse in vitro. *Biomaterials* **1996**, *17*, 1949–1954. [CrossRef]

93.  Puleo, D.A.; Huh, W.W. Acute toxicity of metal ions in cultures of osteogenic cells derived from bone marrow stromal cells. *J. Appl. Biomater.* **1995**, *6*, 249–258. [CrossRef] [PubMed]

94.  Available online: http://www.kokusen.go.jp/pdf/n-20190314_1.pdf (accessed on 4 May 2019).

95.  Schierano, G.; Mussano, F.; Faga, M.G.; Menicucci, G.; Manzella, C.; Sabione, C.; Genova, T.; von Degerfeld, M.M.; Peirone, B.; Cassenti, A.; et al. An alumina toughened zirconia composite for dental implant application: In vivo animal results. *Biomed. Res. Int.* **2015**, *2015*, 157360. [CrossRef] [PubMed]

96.  Piconi, C.; Sandri, M. New materials for dental implantology. *Key Eng. Mater.* **2017**, *750*, 189–194. [CrossRef]

97.  Kohal, R.-J.; Att, W.; Baechle, M.; Bitz, F. Ceramic abutments and ceramic oral implants. An update. *Periodontology 2000* **2008**, *47*, 224–243. [CrossRef] [PubMed]

98.  Oda, Y.; Miyatake, S.; Tokuriki, Y.; Handa, H. Alumina-ceramics (Bioceram) as the implant material in anterior cervical fusion. *Nihon Geka Hokan* **1981**, *50*, 352–357. [PubMed]

99.  Mostofi, K.; Moghaddam, B.G.; Peyravi, M.; Khouzani, R.K. Preliminary results of anterior cervical arthroplasty by porous alumina ceramic cage for cervical disc herniation surgery. *J. Craniovertebral. Junction Spine* **2018**, *9*, 223–226. [CrossRef] [PubMed]

100. McEntire, B.J.; Enomoto, Y.; Zhu, W.; Boffelli, M.; Marin, E.; Pezzotti, G. Surface toughness of silicon nitride bioceramics: II, Comparison with commercial oxide materials. *J. Mech. Behav. Biomed. Mater.* **2016**, *54*, 346–359. [CrossRef]